Article
Beitr. Phys. Atmosph., February 1995, p. 15–41
0005-8173/95/01 0015–27 $ 3.00/0
Vol. 68, No. 1 15

The Non-Hydrostatic Mesoscale Model GESIMA. Part II: Parameterizations and Applications

by D. P. EPPEL, H. KAPITZA, M. CLAUSSEN[1], D. JACOB[1], W. KOCH, L. LEVKOV, H.-T. MENGELKAMP and N. WERRMANN

GKSS-Forschungszentrum, 21502 Geesthacht, Germany
[1]Present address: Max-Planck-Institut für Meteorologie, Bundesstr. 55, 20146 Hamburg, Germany

(Manuscript received May 15, 1993; accepted October 5, 1994)

Abstract

The physical parameterizations implemented in the reference version of the non-hydrostatic mesoscale model GESIMA (= Geesthacht Simulation Model of the Atmosphere) are presented and discussed, namely the turbulent diffusion, the cloud physics, the radiative transfer, and the lower boundary treatment (energy budget). Three different applications show satisfactory agreement with either measurements or physical reasoning.

Zusammenfassung

Das nicht-hydrostatische Mesoskalen-Modell GESIMA. Teil II: Parameterisierungen und Anwendungen

Die physikalischen Parameterisierungen, die in der Referenzversion des nicht-hydrostatischen Mesoskalen-Modells GESIMA (= Geesthacher Simulationsmodell der Atmosphäre) implementiert sind, werden vorgestellt und erläutert. Dazu gehören insbesondere die turbulente Diffusion, die Wolkenphysik, die Strahlungsübertragung und die untere Randbehandlung mit Hilfe einer Energiebilanz. Für drei verschiedene Anwendungen ergeben sich zufriedenstellende Übereinstimmungen sowohl mit Messungen als auch mit theoretischen Überlegungen.

1 Introduction

This sequel paper on the nonhydrostatic mesoscale model GESIMA of Kapitza and Eppel (1992), subsequently referred to as KE92, describes the physical parameterizations used as reference implementations for standard applications.

The rationale behind the specific choices described below is on the one hand the expectation to have a versatile tool for attacking problems such as impact studies on the environment due to existing and/or projected human activities. On the other hand climate models need subgrid scale parameterizations which should be derived from small scale information not directly available by the coarse-resolution climate models. Mesoscale models are expected to bridge this gap. However, it remains to be seen if the parameterizations obtained from mesoscale models are sufficient for climate predictions. Still these 'derived' parameterizations would be used in a more or less 'statical' way as the values of subgrid scale fluxes would be (and are) calculated in terms of the variables of the coarse climate models. This last remark points to an application of mesoscale models from which progress has come and further progress is expected not only in short term predictions but also in climate research: mesoscale models can be used to a certain extent as sophisticated intermediate scale models by nesting into a coarser circulation model. In this way the range of scales over which the energy flow is determined dynamically can be considerably extended.

With the above fields of application in mind GESIMA has been set up in a highly modular structure such that the parameterization modules presented here can easily be replaced by more elaborate ones.

In Chapter 2 the description of the turbulence parameterization is given, followed by overviews of

the cloud module used (Chapter 3), of the radiative transfer routine (Chapter 4), and of the surface energy budget algorithm (Chapter 5). Chapter 6 contains applications. A separate section is devoted to the procedure of initialization used so far. The applications are chosen to show the strengths and shortcomings of the main components of the reference code. The simulation of an episode of the Øresund experiment gives insight into the performance of the turbulence parameterization when applied to a land-sea environment. The calculation of a sea-breeze event shows how cloud formation is treated in the model, and finally, the simulation of heavy metal transport in a coastal area gives an impression on the capability of GESIMA when applied to pollutant transport.

2 Turbulent Diffusion

The amount of sophistication put into subgrid-scale or turbulence parameterization strongly depends on the time limitations dictated by the computing power resources available. For the model to run on a supercomputer, and in order not to unduly limit the other parameterizations, the turbulence model is restricted to one additional dynamical equation. Despite the deficiencies this approximation has, it is regarded appropriate to catch the essential features of a dynamically changing turbulent flow field: advection of turbulent energy by the average flow, creation of turbulence by shear, creation or destruction of turbulence by buoyancy, redistribution of turbulent energy by diffusion, and decay by dissipation.

The turbulent momentum fluxes are calculated by a first order closure scheme according to level 2.5 in the hierarchy of Mellor and Yamada (1974), which can be written using tensor notation:

$$\tau_{ij} := -\langle u_i' u_j' \rangle = K_{ij}\left(\frac{\partial u_i}{\partial x_j} + \frac{\partial u_j}{\partial x_i}\right)$$

$$= K_{ij} \sum_{k=1}^{3} \left(\frac{\partial u_i}{\partial \xi_k}\frac{\partial \xi_k}{\partial x_j} + \frac{\partial u_j}{\partial \xi_k}\frac{\partial \xi_k}{\partial x_i}\right). \qquad (2.1)$$

u_i' is the deviation from the mean Cartesian velocity component in the coordinate direction x_i, ξ_k is the k-th component of the transformed coordinate system, and K_{ij} denotes the turbulent momentum exchange coefficient tensor. For transformation rules see KE92.

The momentum exchange coefficient tensor K_{ij} is approximated by only two coefficients, namely a vertical coefficient $K_{M3} = K_{i3} = K_{3i}$ (i = 1, 2, 3) and a horizontal coefficient $K_{M1} = K_{ij}$ (i, j = 1, 2). The vertical coefficient is assumed to be a function of turbulent kinetic energy, e:

$$K_{M3} = c_0 l_m e^{0.5} \qquad (2.2)$$

($c_0 = 0.4$). The mixing length l_m is calculated according to Blackadar (1962):

$$l_m(z) = \frac{1}{\Phi_M} \cdot \frac{\kappa z}{1 + \frac{\kappa z}{\lambda}} \qquad (2.3)$$

where $\kappa = 0.35$, and the maximum mixing length λ is chosen proportional to the first vertical moment of turbulent kinetic energy (Mellor and Yamada, 1974):

$$\lambda = 0.1 \frac{\int_0^\infty e z\, dz}{\int_0^\infty e\, dz}. \qquad (2.4)$$

The stability function Φ_M is taken from Businger et al. (1971):

$$\Phi_M(z) = \begin{cases} 1 + 4.7\frac{z}{L} & \text{for } z/L \geq 0 \\ \left(1 - 15\frac{z}{L}\right)^{-0.25} & \text{for } z/L < 0. \end{cases} \qquad (2.5)$$

L denotes the Monin-Obukhov length scale. The scaled height, (z/L), is calculated as a function of the Richardson number Ri defined by

$$Ri = \frac{\frac{g}{\Theta}\frac{\partial \Theta}{\partial z}}{\left(\frac{\partial u}{\partial z}\right)^2 + \left(\frac{\partial v}{\partial z}\right)^2}. \qquad (2.6)$$

Following Blanc (1982), one has for $-1.5 \leq Ri \leq -0.01$:

$$\frac{z}{L} \approx -10^{(c_1 + c_2 + c_3)} \qquad (2.7)$$

with

$$c_1 = 0.0284$$
$$c_2 = 0.9612\,(\log(-Ri)) \qquad (2.8)$$
$$c_3 = 0.0013\,(\log(-Ri))^2.$$

The coefficients c_i are found by fitting a polynomial to the solution of the inverted equation Ri = f (z/L) in Businger et al. (1971).

For $-0.01 < Ri \leq 0$ one has approximately

$$\frac{z}{L} \approx 1.3\,Ri \tag{2.9}$$

and for $0 < Ri \leq 0.20$:

$$\frac{z}{L} = \frac{-d_2 - (d_2^2 - 4d_1d_3)^{0.5}}{2d_1}. \tag{2.10}$$

The coefficients d_i are components of a quadratic polynomial solution of the inverted equation $Ri = f(z/L)$, given by

$$\begin{aligned} d_1 &= 22.09\,Ri - 4.7 \\ d_2 &= 9.4\,Ri - 0.74 \\ d_3 &= Ri. \end{aligned} \tag{2.11}$$

The vertical exchange coefficient for heat, for water in all phases and for passive constituents, K_{H3}, is set proportional to the coefficient for momentum:

$$K_{H3} = Pr^{-1} K_{M3}. \tag{2.12}$$

The factor of proportionality is the inverse of the Prandtl number Pr (Businger et al., 1971):

$$Pr^{-1} = \begin{cases} \dfrac{1 + 4.7\,\dfrac{z}{L}}{0.74 + 4.7\,\dfrac{z}{L}} & \text{for } z/L \geq 0 \\[2ex] \dfrac{1.35 \cdot \left(1 - 9\,\dfrac{z}{L}\right)^{0.5}}{\left(1 - 15\,\dfrac{z}{L}\right)^{0.25}} & \text{for } z/L < 0. \end{cases} \tag{2.13}$$

The horizontal exchange coefficients K_{M1} and K_{H1} are set proportional to the vertical coefficients K_{M3} and K_{H3}, respectively:

$$\begin{aligned} K_{M1} &= 2.3\,K_{M3} \\ K_{H1} &= 2.3\,K_{H3}. \end{aligned} \tag{2.14}$$

For applications in the mesoscale-β range (phenomena with horizontal scales of at least 10 km) the aspect ratio, defined here as the ratio between the vertical and the horizontal length scale, is generally much smaller than unity. In that case some simplifications are possible: For the vertical momentum diffusion terms represented by τ_{i3} for $i = 1, 2, 3$ the horizontal derivatives in Eq. (2.1) are small compared to the vertical derivatives due to the small aspect ratio assumption. Therefore, the horizontal derivatives can be neglected. The horizontal momentum diffusion terms represented by τ_{ij} with $i = 1, 2, 3$ and $j = 1, 2$ are not calculated explicity in the small aspect ratio case. Instead, a numerical filter is applied in the horizontal coordinate directions. This filter is implemented as a second or fourth order diffusion (controlled by a switch) with a constant coefficient adjusted such that small scale noise due to the aliasing effect is suppressed. Formally, the turbulent momentum flux tensor becomes asymmetric by this procedure since τ_{31} and τ_{32} are defined differently than τ_{13} and τ_{23}. However, this is justified as long as the aspect ratios of the applications considered are much smaller than unity because horizontal derivatives of τ_{31} and τ_{32} are used in Eq. (2.18c) of KE92, while vertical derivatives of τ_{13} and τ_{23} are used in Eqs. (2.18a) and (2.18b) of KE92, respectively. The horizontal exchange coefficients K_{H1} are replaced by a horizontal filter in analogy to the treatment of the momentum equations. All applications presented in Chapter 6 make use of the small aspect ratio assumption.

The equation for turbulent kinetic energy is simplified by neglecting the production terms due to horizontal shear since the horizontal gradients are weighted by the aspect ratio. These contributions are assumed to be at least one order of magnitude smaller than the vertical shear production (Bougeault and Lacarrere, 1989). The final equation in transformed coordinates is:

$$\begin{aligned} &\frac{\partial}{\partial t}(J\bar{\rho}e) + \nabla_\xi \cdot (\mathbf{F}e) \\ &= -J\tau_{13}\zeta_z\frac{\partial u}{\partial \zeta} - J\tau_{23}\zeta_z\frac{\partial v}{\partial \zeta} + \frac{\partial}{\partial \zeta}\left(J\bar{\rho}\alpha_e K_{M3}\zeta_z^2\frac{\partial e}{\partial \zeta}\right) \\ &\quad - \frac{J\bar{\rho}g}{\Theta}K_{H3}\zeta_z\frac{\partial \Theta}{\partial \zeta} - c_\varepsilon\frac{J\bar{\rho}e^{1.5}}{l_m} \end{aligned} \tag{2.15}$$

($c_\varepsilon = 0.064$, $\alpha_e = 1.0$). For details of the coordinate transformation see KE92. Eq. (2.15) is restricted to relatively flat terrain due to the small aspect ratio assumption.

3 Cloud Parameterization

The temporal scales of mesoscale models are beyond the range on which microphysical cloud processes take place. Additionally, the spatial scales do not allow to resolve individual convective clouds. Therefore, a Kessler type bulk formulation for the formation of cloud water (q_l), rain water (q_r) and cloud ice (q_i) from water vapour (q_v) (Kessler, 1969) is chosen with extensions from Lin et al. (1983) and Orville and Kopp (1977). The parame-

terization is necessarily scale-dependent, and some assumptions apply. All parameterization formulas are strictly presented in mks-units.

A parameterization of the microphysical processes associated with the ice phase is more complicated than the liquid phase physics. The processes are highly dependent on the temperature, the local supersaturation and the forms of the ice crystals. In the scheme presented here only one effective low density ice, i.e. snow, is considered. As a consequence, it is assumed that the ice particles grow fast enough to always have a non-zero terminal velocity. Differences in form, structure and size of ice crystals are not taken into account.

For rain drops and snow crystals a size distribution is assumed according to Marshall and Palmer (1948) and Gunn and Marshall (1958):

$$\begin{aligned} n_r(D) &= n_{0r} \cdot \exp(-\lambda_r D) \\ n_i(D) &= n_{0i} \cdot \exp(-\lambda_i D) \end{aligned} \tag{3.1}$$

with the intercept parameters $n_{0r} = 8 \cdot 10^6\,\mathrm{m}^{-4}$ and $n_{0i} = 3 \cdot 10^6\,\mathrm{m}^{-4}$. $n_r(D)$ and $n_i(D)$ give the number of raindrops and ice crystals, respectively, per unit volume and per unit interval centered around diameter D. The distribution parameters λ_r and λ_i are found by integrating the densities of all rain and ice particles (assuming spherical form for both) over all diameters and equating the result to their mass densities $\bar{\rho} q_r$ and $\bar{\rho} q_i$, respectively, which yields

$$\begin{aligned} \lambda_r &= \left(\frac{\pi \rho_r n_{0r}}{\bar{\rho} q_r} \right)^{0.25} \\ \lambda_i &= \left(\frac{\pi \rho_i n_{0i}}{\bar{\rho} q_i} \right)^{0.25} \end{aligned} \tag{3.2}$$

with the bulk densities of water $\rho_r = 1000\ \mathrm{kg/m}^3$ and of ice $\rho_i = 100\ \mathrm{kg/m}^3$.

Cloud droplets and rain drops are assumed to have the same temperature as the surrounding air. Therefore, they are not contributing to the energy transport (Lord et al., 1984). This assumption is in contrast to Orville and Kopp (1977).

It is further assumed that turbulent mixing in clouds takes place on a shorter time scale than is resolved by the mesoscale model leading to a homogeneous distribution of the cloud components inside a grid box. Each grid box is either completely cloud covered or cloud free, an assumption which, at the moment, restricts the horizontal grid resolution to at most 5 km for the simulation of episodes with cloud activity.

The set of equations in transformed coordinates derived in KE92 (their equations (2.18)–(2.20)) is modified in order to allow for cloud physics. The equation for z-momentum ((2.18c) in KE92) receives an additional term $-J\bar{\rho}g(q_l + q_i + q_r)$ on the right hand side representing the body force arising from the load with liquid water and ice crystals. The equation for potential temperature ((2.19) in KE92) is augmented with a source/sink term $+J\bar{\rho}Q_\theta$ on the right hand side representing heating/cooling due to phase transitions. The exact form of Q_θ is described below in more detail. Four prognostic equations for water vapor mixing ratio q_v, for cloud water mixing ratio q_l, for cloud ice mixing ratio q_i, and for rain water mixing ratio q_r, respectively, are added to the system:

$$\begin{aligned} &\frac{\partial}{\partial t}(J\bar{\rho} q_j) + \nabla_\xi \cdot (\mathbf{F} q_j) \\ &= \nabla_\xi \cdot (\bar{\rho} \Sigma_{q_j}) + \nabla_\xi \cdot (\mathbf{F}_{s,j}\, q_j) + J\bar{\rho} Q_{q_j}, \\ &j = v, l, r, i. \end{aligned} \tag{3.3}$$

The first term on the right hand side is the divergence of the turbulent flux vector, the second term is the divergence of the sedimentation flux, and the third term represents sources and sinks. Σ_{q_j} is defined by

$$\Sigma_{q_j} = -J \begin{Bmatrix} \xi_x & \xi_y & \xi_z \\ \eta_x & \eta_y & \eta_z \\ \zeta_x & \zeta_y & \zeta_z \end{Bmatrix} \cdot \begin{Bmatrix} \langle u' q_j' \rangle \\ \langle v' q_j' \rangle \\ \langle w' q_j' \rangle \end{Bmatrix}. \tag{3.4}$$

$\mathbf{F}_{s,j}$ is defined in analogy to the contravariant mass fluxes $\mathbf{F}$ from KE92 as

$$\mathbf{F}_{s,j} = J\bar{\rho} \begin{Bmatrix} \xi_z V_j \\ \eta_z V_j \\ \zeta_z V_j \end{Bmatrix} \tag{3.5}$$

with the terminal fall velocity V_j of quantity q_j. Note that by convention V_j is always positive. Cloud droplets are considered sufficiently small to set V_l to zero. Also, water vapor is a gas and consequently V_v is zero. For rain we use the parameterization of the mass-weighted mean terminal velocity given by Kessler (1969):

$$V_r = 90.8 \left(\frac{\bar{\rho} q_r}{n_{0r}} \right)^{0.125} \left(\frac{\rho_0}{\bar{\rho}} \right)^{0.5} \tag{3.6}$$

where ρ_0 is the sea level reference density. The rain fall rate R_r in mm/h is then calculated from

$$R_r = 3.6 \cdot 10^6 q_r V_r \left(\frac{\bar{\rho}}{\rho_r} \right). \tag{3.7}$$

For the ice crystal terminal velocity V_i we use the parameterization given by Lin et al. (1983), which is

$$V_i = \frac{c\Gamma(4+d)}{6\lambda_i^d}\left(\frac{\rho_0}{\bar{\rho}}\right)^{0.5} \tag{3.8}$$

with the constants $c = 4.836\ m^{1-d}\ s^{-1}$ and $d = 0.25$. Γ is the Gamma-function. The snow fall rate R_i in mm/h can be found in analogy to Eq. (3.7):

$$R_i = 3.6 \cdot 10^6 q_i V_i \left(\frac{\bar{\rho}}{\rho_i}\right). \tag{3.9}$$

The transformation rates Q_{q_j} from Eq. (3.3) are grouped into three temperature ranges: for $T > T_0 = 0\ °C$ cloud water exists and snow melts. In the range $T < T_{00} = -35\ °C$ cloud water freezes instantaneously and only ice clouds can exist. In the intermediate range $T_{00} < T < T_0$ both cloud components can coexist and exchange matter and energy.

In order to allow for the coexistence of liquid and ice phase the supersaturation is determined with respect to water and ice surfaces. The saturation vapor mixing ratio q_v^* in a grid volume is calculated as the mass-weighted average of the respective saturation values over liquid water q_l^* and over ice q_i^*:

$$q_v^* = \frac{q_l q_l^* + q_i q_i^*}{q_l + q_i}, \qquad q_l^* = \frac{0.622\, e_l}{p - e_l}, \quad q_i^* = \frac{0.622\, e_i}{p - e_i} \tag{3.10}$$

Empirical formulae for the saturation water vapor pressure with respect to liquid water, e_l, and with respect to ice, e_i, are taken from Murray (1967):

$$e_l \simeq 610.78 \exp\left[\frac{17.269\,(T - 273.16)}{T - 35.86}\right],$$

$$e_i \simeq 610.78 \exp\left[\frac{21.875\,(T - 273.16)}{T - 7.66}\right], \tag{3.11}$$

with the temperature T given in K.

The physical processes constituting the transformation rates are depicted schematically in Figure 1 and their meaning can be found in the List of Symbols. For the different temperature ranges the following compositions of source terms for the individual cloud variables and for potential temperature are used ($p_{00} = 10^5$ Pa):

Range A: $T > T_0$:

$$\begin{aligned} Q_{q_v} &= -Q_{CN} + Q_{EV} \\ Q_{q_l} &= +Q_{CN} - Q_{RAC} - Q_{AU} - Q_{SAC} \\ Q_{q_r} &= -Q_{EV} + Q_{RAC} + Q_{AU} - Q_{MS} \\ Q_{q_i} &= +Q_{SAC} + Q_{MS} \end{aligned} \tag{3.12}$$

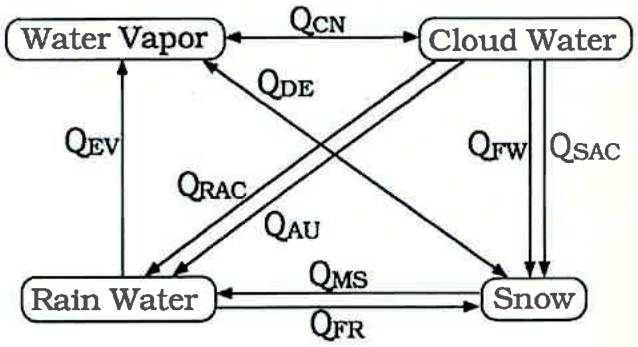

Figure 1 Schematic representation of cloud microphysical processes between the different reservoirs of water (see List Symbols for definition of the processes).

$$Q_\theta = \left(\frac{p_{00}}{p}\right)^{\frac{R}{c_p}} \left[\frac{L_C}{c_p}(Q_{CN} - Q_{EV}) + \frac{L_F}{c_p} Q_{MS}\right] \tag{3.13}$$

Range B: $T_{00} \le T \le T_0$

$$\begin{aligned} Q_{q_v} &= -Q_{CN} + Q_{EV} - Q_{DE} \\ Q_{q_l} &= +Q_{CN} - Q_{RAC} - Q_{AU} - Q_{SAC} \\ Q_{q_r} &= -Q_{EV} + Q_{RAC} + Q_{AU} - Q_{FR} \\ Q_{q_i} &= +Q_{DE} + Q_{SAC} + Q_{FR} \end{aligned} \tag{3.14}$$

$$Q_\theta = \left(\frac{p_{00}}{p}\right)^{\frac{R}{c_p}} \left[\frac{L_C}{c_p}(Q_{CN} - Q_{EV}) + \frac{L_S}{c_p} Q_{DE} + \frac{L_F}{c_p}(Q_{SAC} + Q_{FR})\right] \tag{3.15}$$

Range C: $T \le T_{00}$

$$\begin{aligned} Q_{q_v} &= -Q_{DE} \\ Q_{q_l} &= -Q_{SAC} - Q_{FW} \\ Q_{q_r} &= -Q_{FR} \\ Q_{q_i} &= -Q_{DE} + Q_{SAC} + Q_{FW} + Q_{FR} \end{aligned} \tag{3.16}$$

$$Q_\theta = \left(\frac{p_{00}}{p}\right)^{\frac{R}{c_p}} \left[\frac{L_S}{c_p} Q_{DE} + \frac{L_F}{c_p}(Q_{FW} + Q_{FR})\right]. \tag{3.17}$$

A description of the individual microphysical processes grouped into transformation rates and into adjustment terms follows.

a) Transformation Rates

Autoconversion Rate, Q_{AU}

Autoconversion describes the process of generating large droplets classified as rain by the fusion of smaller cloud droplets. Berry (1967, 1968) suggested a parameterization formula for the autoconversion rate as a function of the number concentration of cloud droplets, N [m^{-3}], and the relative dispersion

coefficient of the droplet distribution, $\nu = 0.28$, at initial time. ν allows to control the general type of cloud going to be simulated. The value used here is valid for maritime cumulus type clouds. In principle ν gives only the initial relative dispersion of the droplet spectrum, but for simplicity we assume it to be a constant throughout the simulation time. Berry's relation is

$$Q_{AU} = \frac{1}{10^3 \bar{\rho}} \cdot \frac{(10^3 \bar{\rho} q_l)^2}{60\left(2 + \frac{0.0266}{\nu} \cdot \frac{10^{-6} N}{10^3 \bar{\rho} q_l}\right)}. \quad (3.18)$$

The cubic dependence of Q_{AU} on the cloud water content q_l results from solving an equation for the time development of a cloud droplet spectrum. The influence of the composition of the air mass on the number of cloud droplets N is taken into account by using an iterative procedure to determine N, which is described in detail in Jacob (1991).

Evaporation of Rain Water, Q_{EV}

According to Ogura and Takahashi (1971) the evaporation rate for rain drops is

$$Q_{EV} = \frac{1}{10^{-3} \bar{\rho}} \cdot \frac{f_v\left(1 - \frac{q_v}{q_l^*}\right)(10^{-3} \bar{\rho} q_r)^{0.525}}{5.4 \cdot 10^5 + \frac{0.41 \cdot 10^7}{10^{-2} e_l}}. \quad (3.19)$$

Depending on their terminal velocity and the amount of subsaturation rain drops are evaporating partly or completely while falling into subsaturated regions. This process is taken into account in Eq. (3.19) through the ventilation factor f_v:

$$f_v = 1.6 + 0.57 \cdot V_r^{1.5}, \quad (3.20)$$

where Kessler's (1969) terminal fall velocity for rain drops (Eq. (3.6)) is inserted. An additional coefficient f_0^{-1} in the original formula of Ogura and Takahashi (1971) is dropped since the falling particles consist of water for which $f_0 = 1$. f_0 represents the terminal fall velocity reduction of ice particles compared to rain drops of the same size.

Freezing of Rain Water, Q_{FR}

The rate equation for raindrop freezing is based on the work by Bigg (1953). The formation of ice particles is considered due to immersion freezing, i.e. nucleation of a supercooled droplet by an ice nucleus suspended in the droplet. The freezing rate (see Lin et al., 1979) is written as

$$Q_{FR} = 20\pi^2 B' n_{0r} \frac{\rho_w}{\bar{\rho}} \cdot (e^{(A'(T_0 - T))} - 1) \cdot \lambda_r^{-7}, \quad (3.21)$$

with the constants $A' = 0.66\,K^{-1}$ and $B' = 100\,m^{-3}s^{-1}$.

Freezing of Cloud Water, Q_{FW}

At temperatures below – 35 °C the total amount of cloud water is freezing homogenously and instantaneously to ice (Lord et al., 1984):

$$Q_{FW} = \frac{q_l}{\Delta t} \quad (3.22)$$

where Δt is the time step of the model.

Melting Rate, Q_{MS}

Below the melting level the melting rate is dependent on the temperature and the saturation mixing ratio according to Lin et al. (1983). This allows the melting process to be slow. It may even take a few time steps of the model. In contrast to Lin et al. (1983) we neglect the increase of the melting rate due to accreted water. The resulting formula is:

$$Q_{MS} = \frac{-2\pi n_{0i}}{\bar{\rho} L_F}[K_a(T - T_0) - L_C \Psi \bar{\rho}(q_i^* - q_v)] \quad (3.23)$$
$$\cdot \left[0.78 \lambda_i^{-2} + 0.31 S_c^{0.333} \Gamma\left(\frac{d+5}{2}\right)\left(\frac{c}{\nu_k}\right)^{0.5}\left(\frac{\rho_0}{\bar{\rho}}\right)^{0.25} \lambda_i^{-(d+5)/2}\right].$$

The two terms in the first pair of brackets on the right hand side describe the diffusion of heat to the surface of the crystal with $T_0 = 0$ °C and the diffusion of water vapor away from the surface of the crystal, respectively. Both of them are modified with a ventilation coefficient for snow flakes, the factor being equal for heat and mass. The parameters are given in the List of Symbols.

Rain Accretion Rate, Q_{RAC}

Coalescence of rain drops with cloud droplets increases rain water and diminishes cloud water. The time development of the coalescence is parameterized following Kessler (1969):

$$Q_{RAC} = 6.96 \cdot 10^{-4} E_c n_{0r}^{0.125} q_l (10^3 \bar{\rho} q_r)^{0.875}\left(\frac{\rho_0}{\bar{\rho}}\right)^{0.5}. \quad (3.24)$$

$E_c \simeq 1$ is the collection efficiency of rain for cloud water, and n_{0r} is the intercept parameter of the Marshall-Palmer drop size distribution function.

Snow Accretion Rate, Q_{SAC}

Accretion of snow by cloud droplets will increase the snow content. According to Lin et al. (1983) we have for the accretion rate:

$$Q_{SAC} = \frac{\pi E_S n_{0i} c \Gamma(3+d)\, q_l}{4\lambda_i^{3+d}} \left(\frac{\rho_0}{\bar{\rho}}\right)^{0.5}. \qquad (3.25)$$

$E_S = 1$ (Schlamp et al., 1975) is the collection efficiency of snow for cloud water. Accretion of rain water by snow is not taken into account. Above the freezing point, collisions of cloud droplets with snow flakes initiate melting.

b) Adjustment Terms

Condensation and Deposition, Q_{CN} and Q_{DE}

The calculation of the amounts of water vapor to be transformed to cloud water and/or ice follows a method described by Lord et al. (1984). After all transformation rates described above have been applied to the cloud variables an adjustment scheme modifies the amounts of water vapor, cloud water and cloud ice such that within an existing cloud the environment is saturated, and in cloud-free regions any supersaturation initiates a cloud. All phase changes are assumed to be isobaric. The exact amounts of water vapor to be condensed to water or deposited to ice are determined with a discrete Newton method. For a trial step size of water vapor change the corresponding temperature and saturation vapor mixing ratio changes are calculated. The resulting mismatch is used to determine a correction, after which a new iteration is started. Experience shows that 3–5 iterations are sufficient.

For the temperature range B a special assumption is necessary which specifies how the available water vapor change is distributed between liquid water and ice. Following Lord et al. (1984) we assume for supersaturated conditions a linear dependence of the production terms on the temperature:

$$\Delta q_l = -\Delta q_v \left(\frac{T - T_{00}}{T_0 - T_{00}}\right)$$
$$\Delta q_i = -\Delta q_v \left(\frac{T_0 - T}{T_0 - T_{00}}\right). \qquad (3.26)$$

For subsaturated conditions we assume that the evaporation process is much faster than sublimation. This is realized by enforcing that first only liquid water evaporates. If all cloud water has been removed and the cloud environment is still subsaturated, sublimation of ice starts. Given the increments found from the iterative adjustment procedure the production rates can be written as:

$$Q_{CN} = \frac{\Delta q_l}{\Delta t}$$
$$Q_{DE} = \frac{\Delta q_i}{\Delta t}. \qquad (3.27)$$

The parameterization scheme has been tested in different environments. Simulations of clouds and rain in the vicinity of Hawaii (Joint Hawaiian Warm Rain Project), of warm maritime tropical cumulus clouds during GATE (GARP Atlantic Tropical Experiment within the intertropical convergence zone), and of organized convection in mid-latitudes during KonTur (Convection and Turbulence Experiment over the North Sea) demonstrated that the cloud parameterization describes the evolution of precipitation well. Details are documented in Jacob (1991) and in Levkov et al. (1986, 1989).

4 Radiative Transfer

A radiative transfer scheme to be used in a mesoscale model is expected to supply realistic heating/cooling rates at an affordable computational expense. Therefore, in the long-wave spectral range the radiative transfer equation is solved in the simple two-stream approximation. In the short-wave range only the scattering process is taken into account resulting in a simple parameterization of the solar flux at the surface. This is justified by the dominance of the scattering effect over that of absorption (see discussion below).

Apart from the simplifications needed for the derivation of the two-stream approximation (path elongation factor, scaling method, broad band approximation) the module implemented currently in GESIMA is to be considered as preliminary since short-wave scattering and long-wave absorption due to the presence of trace gases other than water vapor are not yet taken into account. Also, heating/cooling rates at cloud top levels due to absorption processes in the near-infrared spectral region are neglected. As these processes are found to be important under certain weather conditions (Moussiopoulos, 1987) an extended module is being prepared for implementation. The detailed description of the current scheme can be found in Bakan (1994).

a) Short-Wave Radiation

In the short-wave spectral domain only the solar flux at the surface is considered. This flux enters the

surface energy budget described in Chapter 5. The solar flux is found from the position of the sun and from either the amount of cloud cover or from the liquid water path. The zenith angle, ζ_{zen}, of the solar energy-flux vector impinging on a horizontal surface is determined by the relation:

$$\cos(\zeta_{zen}) = \sin(\Phi) \cdot \sin(\delta) + \\ + \cos(\Phi) \cdot \cos(\delta) \cdot \cos(t_H) \quad (4.1)$$

where Φ is the geographical latitude, and δ denotes the declination of the sun which is a function of the day N_d in the year:

$$\sin(\delta) = \sin(\varepsilon) \cdot \sin\left(N_d \frac{2\pi}{365}\right). \quad (4.2)$$

$\varepsilon = 23.45°$ is the angle of the ecliptic of the earth, and N_d is counted in days after the start of spring (March 21st). The local hour angle t_H is defined to be 0° at noon and 180° at midnight. It is related to the local time t_L (given in hours) by

$$t_H = (t_L - 12) \cdot \frac{\pi}{12}. \quad (4.3)$$

Sunrise and sunset times can be found by setting $\zeta_{zen} = 90°$ in Eq. (4.1).

According to Kasten and Czeplak (1980) the solar radiation flux S_0 reaching the surface can be written

$$S_0 = (\bar{S}_0 \cdot \mu - \bar{S}_1) \cdot T_r, \quad (4.4)$$

with $\bar{S}_0 = 950\ W/m^2$, $\bar{S}_1 = 30\ W/m^2$, $\mu = \cos(\zeta_{zen})$, and the shortwave transmission function T_r. The original value of $\bar{S}_0 = 910\ W/m^2$ given by Kasten and Czeplak (1980) has been derived from data taken at a suburban area of Hamburg. Since a lower turbidity is anticipated in most of the applications of GESIMA a new value of $950\ W/m^2$ has been determined from recent measurements near the North Sea coast (Claussen, 1988).

For applications without explicit cloud parameterization the transmission T_r is given by Kasten and Czeplak (1980) as a function of the fractional cloud cover $N_c (0 \le N_c \le 1)$ to be supplied from observations or any other means:

$$T_r = 1 - 0.75 \cdot N_c^{3.4}. \quad (4.5)$$

If cloud development is calculated according to the parameterization presented in Chapter 3 the transmission function is formulated following Stephens (1978):

$$T_r = \frac{1}{1 + \beta_1 \frac{\tau_1}{\mu}}, \quad (4.6)$$

where τ_1 is the optical thickness of the cloud, and β_1 denotes the effective backscatter coefficient given by Stephens (1978) in tabular form as a function of τ_1 and μ. Here, for simplicity, we use an approximation given by Bakan (1994):

$$\beta_1 \sim 0.08 \cdot \mu^{0.5}. \quad (4.7)$$

The optical thickness τ_1 is given by Stephens (1978) as a function of the liquid water path L_w:

$$\tau_1 = 1.8336 \cdot [\lg(10^3 L_w)]^{3.9363}. \quad (4.8)$$

L_w is found by integrating the cloud substance densities from the surface to the model domain top:

$$L_w = \int_{\text{surface}}^{\text{top}} \bar{\rho}\,(q_l + q_i + q_r)\,dz. \quad (4.9)$$

$\bar{\rho}$ is the density of the reference atmosphere, and $q_{l,i,r}$ are the mixing ratios for cloud liquid water, cloud ice, and rain, respectively (see Chapter 3).

For a cloud of $L_w = 0.05\ kg/m^2$ and $\mu = 0.5$ we get $\tau_1 = 14.77$ and $T_r = 0.37$. That is, even for a thin cloud not expected to generate any significant amount of rain the scattering effect results in a solar flux reduction at the surface of 63 %. Considering also absorption can add only a much smaller effect to the surface flux reduction, although it may change the heating/cooling rates at the cloud top significantly.

b) Long-Wave Radiation

In the infrared spectral region the radiation transfer equation is given by

$$\mu \frac{\partial L_\lambda}{\partial z} = -\sigma(L_\lambda - L_{\lambda,B}) \quad (4.10)$$

where $\mu = \cos(\zeta_{zen})$. L_λ denotes the spectral radiation density, $L_{\lambda,B}$ is the source term expressed by the Planck function. The spectral extinction coefficient, σ, also depends on pressure (height) and temperature.

L_λ is a function of the zenith angle, the azimuth angle, and of height. The two-stream approximation transforms Eq. (4.10) into a set of two equations, one for the upward radiation flux $F\uparrow$, and one for the downward radiation flux $F\downarrow$. The transfer equation for $F\uparrow$ is found by multiplying Eq. (4.10) with μ and integrating over the upper half-space $(0 \le \mu \le 1)$ resulting in:

$$\frac{dF\uparrow}{dz} = -\beta \cdot \sigma(F\uparrow - B) \quad (4.11)$$

with the definitions

$$F\uparrow(z) = \int_0^1 \mu L_\lambda d\mu, \quad B = \int_0^1 \mu L_{\lambda,B} d\mu \tag{4.12}$$

and the approximation

$$\int_0^1 \mu^2 \frac{\partial L_\lambda}{\partial z} d\mu \simeq \frac{1}{\beta} \int_0^1 \mu \frac{\partial L_\lambda}{\partial z} d\mu. \tag{4.13}$$

The path elongation factor β takes into account all non-vertically propagating radiation. According to Elsässer (1942) it is set to 1.66.

Approximating the Planck source term $B(z)$ as linear function of height, z,

$$B(z) = B^- + B_z(z - z^-). \tag{4.14}$$

Eq. (4.11) can be solved analytically:

$$F^+_\uparrow = F^-_\uparrow e^{-\beta\sigma\Delta z} + B^+ - \\ - B^- e^{-\beta\sigma\Delta z} - \frac{B_z}{\beta\sigma}(1 - e^{-\beta\sigma\Delta z}). \tag{4.15}$$

Similarly, by integrating Eq. (4.10) over the lower half-space ($0 \geq \mu \geq 1$) one finds a transfer equation for the downward spectral radiation flux $F\downarrow$:

$$F^-_\downarrow = F^+_\downarrow e^{-\beta\sigma\Delta z} + B^- - \\ - B^+ e^{-\beta\sigma\Delta z} + \frac{B_z}{\beta\sigma}(1 - e^{-\beta\sigma\Delta z}). \tag{4.16}$$

In this approximation upward and downward fluxes are only coupled through their values at the upper and lower boundaries.

The mean spectral heating rate in the layer is found from Eqs. (4.15) and (4.16) by calculating the divergence of the net flux F_N:

$$\left.\frac{\partial T}{\partial t}\right|_{\text{spectral}} = -\frac{1}{\rho c_p}\frac{dF_N}{dz} = \\ = -\frac{1}{\rho c_p}\frac{(F^+_\uparrow - F^+_\downarrow) - (F^-_\downarrow - F^-_\uparrow)}{\Delta z}. \tag{4.17}$$

In order to get reliable upper model boundary fluxes ten additional model layers are added on top of the computational domain during the 1-dimensional initialization phase of a model run. Using $F_\downarrow(z^+_{max}) = 0$ as a boundary value, the downward flux at the "true" domain top is calculated for a reference atmosphere. This value is taken as a constant upper boundary value in the subsequent 3-dimensional run.

In order to evaluate the integral over wave numbers a set of spectral intervals is specified where the transmission functions can be approximated realistically (see Rodgers and Walshaw, 1966). In the window region with wavelengths between 8.33 µm and 11.11 µm only the continuum absorption and liquid water absorption are considered.

Following the work of Roberts et al. (1976) and Hollweg (1989), the mass absorption coefficient σ_{cont} is approximately given by

$$\sigma_{cont} \simeq 0.96 \cdot q_v \cdot \exp\left(\frac{1800}{T} - 6.08\right) [m^2 kg^{-1}]. \tag{4.18}$$

For the extinction coefficient of liquid water, results of Buykov and Khvorostyanov (1977) suggest a wavelength independent value of:

$$\sigma_d \simeq 50\ [m^2 kg^{-1}]. \tag{4.19}$$

The Planck function in the window region is approximated by

$$B_w(T) = (0.24 \cdot \exp(0.0163 \cdot T) - 3.934)\ [Wm^{-2}], \tag{4.20}$$

where the coefficients are found from a least squares fit of the true Planck function.

Outside the window region water vapor and liquid water absorption are considered. Currently, the influence of CO_2, O_3 and other trace gases is neglected due to their small contribution to tropospheric heating rates. The transmission $\tilde{T}$ is approximated by a sum of exponential terms adjusted to the results of a statistical band model (see Rodgers and Walshaw, 1966) by tuning the weights a_k:

$$\tilde{T}(m) = \sum_{k=1}^{N_a} a_k e^{-b_k m} \tag{4.21}$$

m is the absorber mass, and N_a is the number of intervals chosen with the corresponding mass absorption coefficients b_k. The volume absorption coefficients are found by multiplying with the water vapor density ρ_v. The weights and absorption coefficients used in GESIMA are listed in Table 1.

Table 1 Weights and absorption coefficients for seven exponential terms.

k	a_k	b_k [m^2/kg]
1	0.0137	4285.0
2	0.0139	605.3
3	0.0994	85.5
4	0.1512	12.08
5	0.1655	1.706
6	0.0922	2.410 · 10–1
7	0.4461	3.404 · 10–2

5 Surface Energy Budget

The calculation of fluxes at the surface is based on a bulk formulation in which latent heat fluxes are calculated by a simple force-restore method, and the sensible ground heat flux is determined by solving a diffusion equation.

Within the first grid box above the ground, the flow is assumed to be in equilibrium with the underlying surface. The surface fluxes, which force the turbulent flow, are evaluated by the requirement that no energy and no mass is stored at the interface between atmosphere and ground. Hence, for the energy fluxes,

$$Q_{rad} + Q_{lat} + Q_{sens} = Q_{ground}. \tag{5.1}$$

The fluxes are considered positive when directed upward. Q_{rad} is the sum of the energy flux densities due to short- and long-wave radiation:

$$Q_{rad} = -S_0(1-\alpha) - F_{\downarrow,G} + \varepsilon_e \sigma_s T_G^4 \tag{5.2}$$

where α and ε_e are the albedo and emissivity of the surface, respectively. The albedo for a land surface is assumed to be a constant parameter dependent only on the land-use characteristics. For a water surface α depends on the zenith angle ζ_{zen} of the sun according to the relation (Claussen, 1988):

$$\alpha_{sea} = 0.25 - 0.23 \cdot \cos(\zeta_{zen}). \tag{5.3}$$

The solar radiation is denoted by S_0 and the longwave counter radiation by $F_{\downarrow,G}$. S_0 is found from Eq. (4.4) as discussed in Chapter 4. $F_{\downarrow,G}$ is calculated from the two-stream approximation of the radiation transfer equation as explained in Chapter 4. T_G is the temperature at the air/ground interface.

Q_{lat} and Q_{sens} are the energy flux densities due to turbulent transports of latent and sensible heat, respectively:

$$Q_{sens} = \rho c_p C_h u(z_1)\,(\Theta_G - \Theta(z_1)) \tag{5.4}$$

$$Q_{lat} = \rho L_C w_e C_q u(z_1)\,(q_{vs,G} - q_v(z_1)) \tag{5.5}$$

where ρ is the density of the air, $u(z_1)$, $\Theta(z_1)$, $q_v(z_1)$ are the velocity, potential temperature, and water vapor mixing ratio at the lowest model level above the surface, respectively. c_p is the specific heat capacity of the air at constant pressure, and L_C is the latent heat of evaporation. C_h and C_q are the transfer coefficients for heat and moisture, respectively, to be defined later in this section.

w_e is a so-called wetness factor. For bare soils, w_e is supposed to be equal to the soil moisture availability m_w (see Claussen, 1988). m_w is the ratio of actual and critical depth w_k of extracted liquid water that a thick upper layer of soil is capable of holding before the soil is saturated. m_w is related to the water vapor mixing ratio $q_{v,G}$ and the saturation mixing ratio $q_{vs,G}$ at the ground by

$$q_{v,G} = m_w q_{vs,G} + (1 - m_w)\, q_v(z_1). \tag{5.6}$$

Here, m_w is computed by a simple force-restore method:

$$\frac{\partial m_w}{\partial t} = -\frac{Q_{lat}/L_C - P}{w_k \rho_w} + \frac{\alpha_c}{\rho_w}(1 - m_w)$$
$$0 \le m \le 1 \tag{5.7}$$

(compare with Deardorff, 1978). ρ_w is the density of water, α_c is a capillarity factor which is basically used to control the water flux from a water table into the upper soil layer. P is the precipitation mass flux. Over vegetated areas, w_e can be restricted by a finite surface or canopy conductance g_s where (see Deardorff, 1978)

$$w_e = \frac{g_s}{g_s + C_q u(z_1)}. \tag{5.8}$$

For g_s a simple model is used:

$$g_s = g_1 g(S_0)\, g(\delta q_v)\, g(T(z_1))\, g(m_w) \tag{5.9}$$

where g_1 is the maximum surface conductance which depends on the type of vegetation. The values of g_1 are taken from Wilson et al. (1987). For wet leaves g_1 is assumed to become infinitly large. The other terms on the right-hand-side of Eq. (5.9), which vary between 0 and 1, account for the reaction of the stomata of plants to solar radiation, water vapor deficit δq_v, actual air temperature $T(z_1)$ and soil moisture, respectively. Here, it is assumed (as a very first approximation) that all plants show the same behavior with respect to their stomata, except for the extreme values g_1. The explicit functional dependence of these terms is given in Dolman (1987), who evaluated the evaporation over an oak forest.

The turbulent momentum flux is parameterized as

$$\tau = \rho C_d u(z_1)^2. \tag{5.10}$$

The transfer coefficients in the Eqs. (5.4), (5.5), and (5.10) are computed from:

$$C_{d,h,q} = \begin{cases} \dfrac{\kappa^2}{\ln\left(\frac{z_p}{z_0}\right)\ln\left(\frac{z_p}{z_0}\right)} F_m \\ \dfrac{\kappa^2}{\ln\left(\frac{z_p}{z_0}\right)\ln\left(\frac{z_p}{z_{0h}}\right)} F_h \\ \dfrac{\kappa^2}{\ln\left(\frac{z_p}{z_0}\right)\ln\left(\frac{z_p}{z_{0q}}\right)} F_q \end{cases} \tag{5.11}$$

where $F_{m,h,q}$ are the stability functions after Louis (1979):

$$F_{m,h,q} = \begin{cases} \dfrac{1}{(1 + 4.7 \cdot \mathrm{Ri})^2} & \text{stable} \\ 1 - \dfrac{9.4 \cdot \mathrm{Ri}}{1 + c_{m,h,q}\sqrt{|\mathrm{Ri}|}} & \text{unstable} \end{cases} \tag{5.12}$$

with the coefficients

$$c_{m,h,q} = c_{0m,h,q}\left(\frac{\kappa}{\ln\left(\frac{z_p}{z_0}\right)}\right)^2 \cdot \sqrt{\frac{z_p}{z_0}} \tag{5.13}$$

and the constants $c_{0m} = 7.4$ and $c_{0h} = c_{0q} = 5.3$.

There is a slight inconsistency in using Eqs. (5.10)–(5.13) instead of integrating for example

$$\frac{\partial U}{\partial z} = \frac{u_*}{\kappa z}\Phi_m\left(\frac{z}{L}\right) \tag{5.14}$$

directly and solving for u_* by iterating. However, this inconsistency is believed to be small since Louis (1979) derived his analytical formulas using $\Phi_{m,h}$ with the objective to avoid the iterations. His comparisons with the iterative results show very good agreement for unstable atmospheric stratification. In the stable regime any turbulent transfer is clipped off for bulk Richardson numbers larger than 0.25.

z_p is the reference height of the transfer coefficients according to Claussen (1990):

$$\ln\left(\frac{z_p}{z_0}\right) = \frac{1}{\Delta z}\int_{z_0}^{\Delta z}\ln\left(\frac{z'}{z_0}\right)dz', \tag{5.15}$$

where Δz is the thickness of the lowest atmospheric layer of the model.

The roughness length z_0 is assumed to be a constant, except for water surface, where z_0 is parameterized by using the Charnock formula (Charnock, 1955) together with Wu's (1982) constant:

$$z_0 = 0.0185 \cdot \frac{u_*^2}{g}. \tag{5.16}$$

The roughness lengths $z_{0h,q}$ depend on the surface characteristics. Following Brutsaert (1979) and Hicks (1985), over surfaces covered with a vegetation or with similar porous or fibrous roughness elements, $\ln(z_0/z_{0h,q})$ is approximately a constant,

$$\ln\left(\frac{z_0}{z_{0h,q}}\right) = 2.3. \tag{5.17}$$

whereas over surfaces with bluff roughness elements $\ln(z_0/z_{0h,q})$ depend on the friction velocity u_* and z_0:

$$\ln\left(\frac{z_0}{z_{0h,q}}\right) = a_{h,q}(u_* z_0)^{0.25} - 2 \tag{5.18}$$

with the constants $a_h = 39.53$ and $a_q = 36.34$.

The heat flux Q_{ground} into the water is taken as the residuum of $Q_{rad} + Q_{sens} + Q_{lat}$. The water temperature is assumed to be a constant $T_G = T_s$ where T_s is a prescribed value. The conductive heat flux into the soil is

$$Q_{ground} = -\lambda_h\left(\frac{\partial T}{\partial z}\right)_{z=0} \tag{5.19}$$

where λ_h is the heat conductivity and T the actual temperature of the soil. The soil temperature is computed from the linear diffusion equation

$$\frac{\partial T}{\partial t} = k\frac{\partial^2 T}{\partial z^2} \tag{5.20}$$

with k as temperature diffusivity.

The surface temperature T_G which corresponds to the balanced fluxes is found by applying an iterative scheme (discrete Newton). The soil layer is discretized in 4 levels with geometrically increasing thickness between 1 cm and about 1 m. The temperature diffusion in the soil is calculated with a semi-implicit method in order to avoid excessively small time steps due to the small thickness of the uppermost layer (1 cm). The algorithm is the same as for the vertical diffusion in the atmosphere described in KE92.

Finally, the dry deposition of trace metals is evaluated from the turbulent flux of the substance in question by

$$F_s = -\rho C_s u(z_1)\, s(z_1), \tag{5.21}$$

where $s(z_1)$ is the mixing ratio of the substance in the lowest model level above the surface. Implicit in Eq. (5.21) is the assumption that the surface or stomatal resistance against small particles is negligibly small (see Voldner et al., 1986); hence, the mean concentration of particles at the air/ground interface should be zero. The transfer coefficient C_s is the same as for temperature, C_h, except that z_{0h} is replaced by a new roughness length z_{0s}. z_{0s} is computed from the resistance due to the viscous sublayer, r_b, by the relation

$$\ln\left(\frac{z_0}{z_{0s}}\right) = \kappa u_* r_b. \tag{5.22}$$

Values of r_b for different land-use categories can be found in Voldner et al. (1986). In principle, r_b is a function of both atmospheric stability and surface roughness resulting in typical diurnal and seasonal cycles: During the day under convective conditions the mixing is much more efficient resulting in smaller resistance compared to the night. According to Voldner et al. (1986) the difference is approximately a factor of 2. The seasonal difference reflects the change of aerodynamical roughness due to snow cover and/or changed vegetation. For winter Voldner et al. (1986) give values of up to one order of magnitude higher than for summer. In GESIMA, only the seasonal differences are taken into account.

GESIMA uses a total of 19 different surface classes given in Table 2. The values of the corresponding characteristic parameters for summer and winter conditions (snow covered ground) are listed in Tables 3 and 4, respectively.

Table 2 Surface classifications

Type	Description
1	North Sea (depth > 10 m)
2	North Sea (depth < 10 m)
3	Baltic Sea
4	Lakes
5	Coniferous forest
6	Mixed forest
7	Deciduous forest
8	Agricultural area (clay, marsh)
9	Agricultural area (sand, moist)
10	Agricultural area (loam, bushes)
11	Agricultural area (sand)
12	Sandbank (dry at regular high tides)
13	Shoals (sandy)
14	Shoals (mixed)
15	Shoals (muddy)
16	Heath
17	Peat mould
18	Urban area
19	City

Table 3 Surface characteristics used for summer simulations.The table entries are: a) temperature diffusivity [10^{-6} m^2/s], b) heat capacity [10^6 $J/(Km^3)$] (note that $\lambda_h = a * b$), c) emissivity ε_e, d) albedo α ("cal" means calculated from other variables), e) roughness length z_0 ("cal" means calculated from other variables) [m], f) field capacity w_k [m], g) capillarity α_c [$kg/(m^3 s)$], h) switch for calculation of $z_{0h,q}$, see Chapter 5 for details, i) maximum evaporation conductivity g_1 [m/s], j) surface resistance for lead particles r_b [s/m].

Type	a	b	c	d	e	f	g	h	i	j
1	0.14	4.2	0.95	cal	cal	1.0	1.0	1	0.0	0.0
2	0.14	4.2	0.95	cal	cal	1.0	1.0	1	0.0	0.0
3	0.14	4.2	0.95	cal	cal	1.0	1.0	1	0.0	0.0
4	0.14	4.2	0.95	cal	cal	1.0	1.0	1	0.0	0.0
5	0.70	2.5	0.95	0.15	0.75	0.01	0.008	0	0.023	190.0
6	0.70	2.5	0.95	0.15	0.75	0.01	0.008	0	0.023	155.0
7	0.70	2.5	0.95	0.15	0.75	0.01	0.008	0	0.023	130.0
8	0.56	2.1	0.95	0.25	0.07	0.01	0.008	1	0.040	400.0
9	0.74	2.9	0.95	0.25	0.17	0.005	0.003	1	0.040	400.0
10	0.73	2.1	0.95	0.25	0.20	0.004	0.002	1	0.040	400.0
11	0.84	2.1	0.95	0.25	0.71	0.003	0.001	1	0.040	400.0
12	0.84	2.1	0.90	0.30	0.0004	0.002	0.0009	1	0.0	270.0
13	0.79	3.2	0.89	0.12	0.0004	1.0	1.0	1	0.0	100.0
14	0.51	3.5	0.91	0.12	0.0004	1.0	1.0	1	0.0	100.0
15	0.45	3.7	0.93	0.12	0.0004	1.0	1.0	1	0.0	100.0
16	0.70	2.5	0.95	0.15	0.35	0.003	0.001	0	0.024	260.0
17	0.45	3.1	0.95	0.15	0.07	0.008	0.006	1	0.024	270.0
18	1.0	2.0	0.90	0.20	0.80	0.003	0.001	1	0.0	270.0
19	1.0	2.0	0.90	0.20	1.2	0.002	0.0009	1	0.0	270.0

6 Applications

In this section several sample applications are documented which test the performance of the complete model system. The first (Øresund-Experiment) focuses on the evaluation of the turbulence parameterization and shows a comparison of turbulence related quantities with aircraft data. The second example (sea-breeze over Schleswig-Holstein) shows the interaction of two sea-breezes

Table 4 Surface characteristics used for winter simulations. The table entries are the same as in Table 3.

Type	a	b	c	d	e	f	g	h	i	j
1	0.14	4.2	0.95	cal	cal	1.0	1.0	1	0.0	0.0
2	0.14	4.2	0.95	cal	cal	1.0	1.0	1	0.0	0.0
3	0.14	4.2	0.95	cal	cal	1.0	1.0	1	0.0	0.0
4	0.14	4.2	0.95	cal	cal	1.0	1.0	1	0.0	0.0
5	0.70	2.5	0.95	0.60	0.50	1.0	1.0	0	0.0	1400.0
6	0.70	2.5	0.95	0.60	0.50	1.0	1.0	0	0.0	1400.0
7	0.70	2.5	0.95	0.60	0.50	1.0	1.0	0	0.0	1400.0
8	0.56	2.1	0.99	0.70	0.001	1.0	1.0	1	0.0	1400.0
9	0.74	2.9	0.99	0.70	0.01	1.0	1.0	1	0.0	1400.0
10	0.73	2.1	0.99	0.70	0.01	1.0	1.0	1	0.0	1400.0
11	0.84	2.1	0.99	0.70	0.01	1.0	1.0	1	0.0	1400.0
12	0.84	2.1	0.99	0.80	0.0001	1.0	1.0	1	0.0	1400.0
13	0.79	3.2	0.99	0.80	0.0001	1.0	1.0	1	0.0	1400.0
14	0.51	3.5	0.99	0.80	0.0001	1.0	1.0	1	0.0	1400.0
15	0.45	3.7	0.99	0.80	0.0001	1.0	1.0	1	0.0	1400.0
16	0.70	2.5	0.95	0.60	0.01	1.0	1.0	0	0.0	1400.0
17	0.45	3.1	0.95	0.60	0.01	1.0	1.0	1	0.0	1400.0
18	1.0	2.0	0.95	0.40	0.80	1.0	1.0	1	0.0	1600.0
19	1.0	2.0	0.95	0.40	1.2	1.0	1.0	1	0.0	1600.0

developing on opposite sides of a narrow land mass. The convergence zone will be traced by the cloud development, which is compared to a satellite image. The third application shows an example of passive constituent transport (lead). The details of all three examples are published elsewhere, so only the main aspects will be presented here. The Øresund case and the lead transport case were calculated with the cloud module turned off since no clouds were observed in both cases. All other parameterizations were used as described in Sections 2–5. First, a brief summary of the initialization process is given.

6.1 Initialization

In order to start a simulation a completely known initial state is needed. It is not recommendable (although possible) to pre-specify the full 3-dimensional fields of all prognostic variables since in general they will not be in balance with the discrete dynamical equations. It is possible to find the balanced state by simple running the model until a steady state is reached. But this is prohibitively expensive with the 3-dimensional model. Therefore, an alternative approach is used: The 3-dimensional model is initialized with a horizontally homogeneous state resulting from a 1-dimensional pre-run. Since inertial oscillations are a main component of the 1-dimensional physics the 1-d run has to simulate several days in order to reach equilibrium. For flat topography the resulting profiles of the 1-d run can be inserted and distributed horizontally into the 3-d domain. If variable topography is present the potential temperature is interpolated to the proper height. The velocities are transformed into mass fluxes through the lateral grid box faces for one reference column. Subsequently, these fluxes are shifted through the domain which automatically satisfies the continuity equation in the 3-d domain (see KE92). All other variables are injected without interpolation.

This procedure generates fairly small disturbances at model start time which damp out within 1 or 2 hours of simulation. Therefore, a gradual buildup of topography (diastrophy) is not necessary. However, it should be kept in mind that this simple initialization method is unsuitable for steep topography since it generates small accelerations proportional to the slope of the grid lines. Instead, a more sophisticated initialization is necessary in that case.

6.2. Øresund-Experiment

The Øresund-Experiment took place in May and June 1984. Details of the campaign are described in Gryning (1985), and the data are available in a data base (Mortensen and Gryning, 1989). The Øresund site, which is the sea area separating Denmark and Sweden, was chosen in order to get insight into the turbulent structure and transport properties of air masses flowing from land over water to land.

For comparison with GESIMA simulations the episode of June 5, 1984 was chosen, as detailed data of turbulent quantities were taken during this time. Since the synoptic situation during the day was essentially stationary with a constant easterly wind blowing till late in the afternoon a constant geostrophical forcing at the upper boundary of the model domain was prescribed. No cloud development was reported. Moreover, since the flow was almost perpendicular to the coast lines showing little variation in cross-wind direction the calculations were performed on a 2-dimensional grid. 40 grid points were used in the horizontal with a constant spacing of 2 km. In the vertical 26 grid boxes were used with variable heights ranging from 6 m at the surface to 500 m at the top which was fixed at 6 km. The water of the Øresund was simulated with grid boxes 19–28, the city of Copenhagen was located at 14–18, while the remaining left and right areas were classified as farmland. Further details can be found in Mengelkamp (1991).

Figure 2 shows the simulated wind speeds at different heights and two selected times together with some measurements. The response to surface roughness and heating shows an acceleration as soon as the wind passes the Swedish coastline due to reduced surface friction over water. A deceleration follows when the Danish land mass is encountered. Near-surface winds decelerate even before the coastline is reached. This effect, also known from observations, is caused by the non-hydrostatic pressure perturbation gradient which develops when air flows from smooth to rough surfaces. The lowest values occur at the downwind end of the high-roughness area of Cogenhagen.

Near-surface winds over water vary in time. During night (0300 CET) a continuous downward momentum flux results in a steady acceleration reducing the vertical wind speed gradient in downwind direction. During daytime (1200 CET) a stable layer has formed over the cold water surface. The atmosphere above this layer is decoupled from the surface and a lower drag results in a continuous wind speed increase. Inside the stable layer, wind speeds gradually decrease because the momentum transfer from above into the surface layer is prevented. Simulation and measurements show an increase of the vertical gradient of wind speed over water in downwind direction.

For the situation simulated and for daytime conditions, a boundary layer structure as shown in Figure 3 is expected. A warm, well-mixed air mass moves from a heated land surface over cooler water

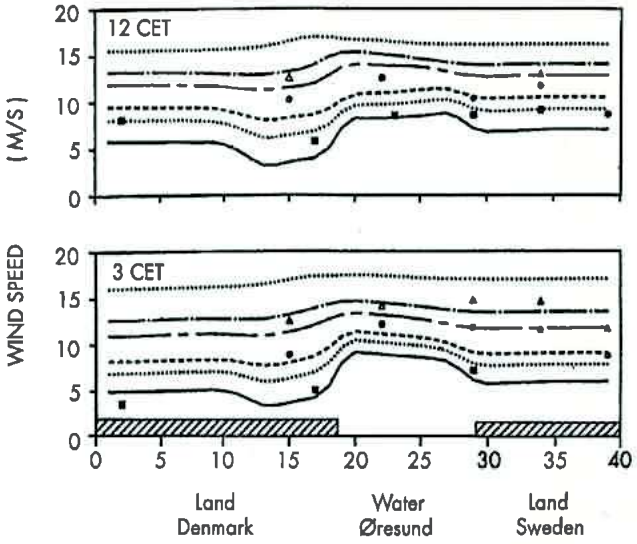

Figure 2 Horizontal profiles of wind speed in the East-West direction at different heights (Bottom to top: 3, 10, 20, 33, 60 and 210 m). Measured data are shown at 10 m (squares), 100 m (dots) and 200 m height (triangles).

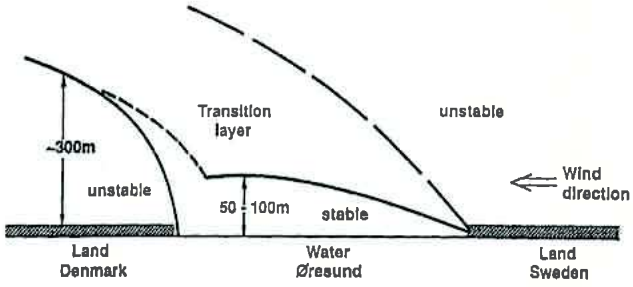

Figure 3 Sketch of turbulence regimes over a land-water-land area with a cold water surface.

onto a second heated land mass with urban surface characteristics. Then a stable internal boundary layer (IBL) forms over water and interacts with the unstable IBL over the city area downwind. Above the stable IBL a transition layer is characterized by decaying turbulence.

As an indicator for turbulence intensity the dissipation rate closely reveals the surface roughness distribution. Figure 4 shows the simulated dissipation rate at different heights together with aircraft measurements. In 14 and 40 m height, an abrupt decrease as the air encounters the water surface is followed by a constant dissipation rate inside the stable layer. The transition layer above is characterized by a continuous decrease until the unstable IBL over the city area is intersected. Airplane measurements performed at 270 m altitude show the overall distribution of turbulence intensity and also its amount in excellent agreement with the simulation.

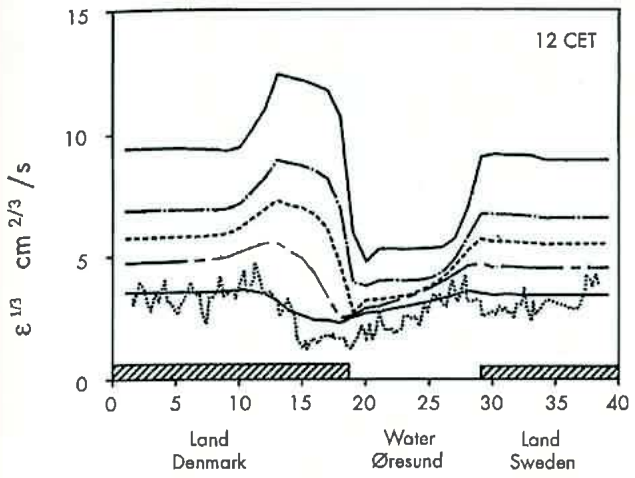

Figure 4 Horizontal profiles of the dissipation rate at different heights (top to bottom: 14, 40, 80, 180 and 320 m). The dotted line represents airplane measurements at 270 m.

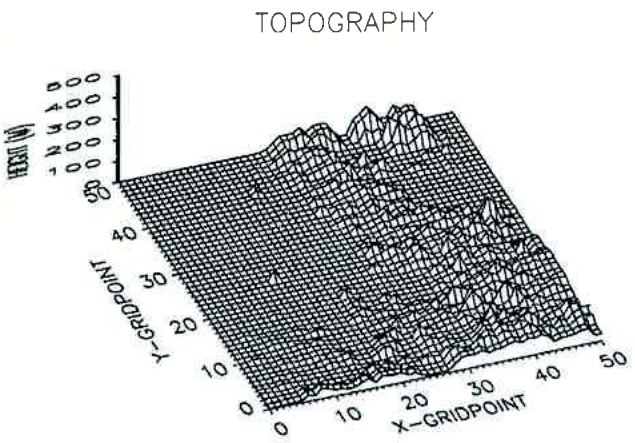

Figure 5 Perspective view of the used orography. The horizontal resolution is 5 km. The maximum elevation is 130 m.

The mixed air is characterized by a high turbulence intensity, decaying turbulence is observed in the transition layer as well as a minimum immediately before an abrupt increase when the unstable IBL over the city is intersected. This point is shown roughly 6 km downwind from the Danish coastline. During night-time (not shown), when a near neutral surface layer developed over water, an increase of the dissipation rate near the surface was simulated in accordance with an increasing wind speed.

The dip occurring in the simulation immediately before the air encounters the Copenhagen area (gridpoints 18–20) reflects a blocking effect typical for flow from a smooth to a rough surface. In an otherwise identical simulation (not shown here), a horizontal resolution of 500 m was used in an area

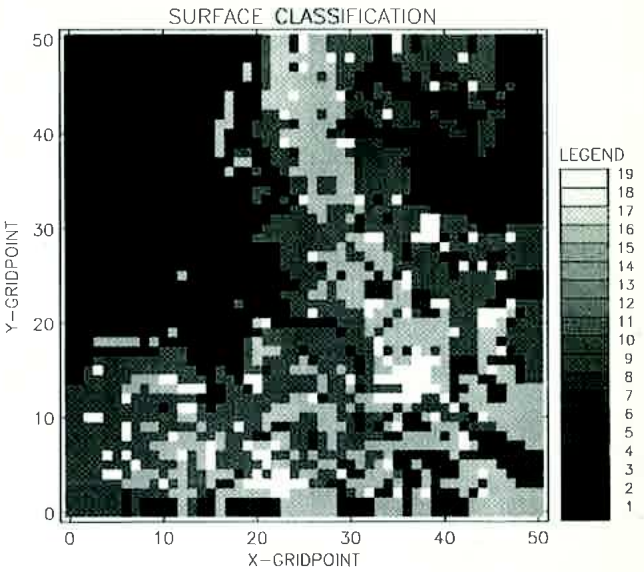

Figure 6 Distribution of surface classes from Table 2 in the solution domain. For clear contrast only 5 classes are displayed: Class 1 ('water') contains surface categories 1, 2, 3, 4, 12, 13, 14 and 15 (flood conditions); class 6 ('forest') contains surface categories 5, 6 and 7; class 10 ('agricultural land, humid') contains surface categories 8, 9 and 10; class 16 ('dry soils') contains surface categories 11, 16 and 17; class 19 ('urban areas') contains surface categories 18 and 19.

of 2 km to both sides of the water-city transition. With this much finer resolution the same behaviour was found stretched over more grid points.

6.3 Sea-Breeze Simulation

The basic dynamics of sea-breeze formation is well understood and will not be repeated here (for overviews and references see Atkinson (1982) and Pielke (1984)). However, due to the complicated land-sea distribution over northern Germany it is not a priori obvious what kind of flow pattern develops given the external forcing.

The solution domain roughly extends from 7° east (island of Norderney) to 11° east (Lübeck) and from 52° north (Bremen) to 55° north (Odense), forming a square with about 250 km side length. The grid resolution in the horizontal is set to 5 km, and the grid spacing in the vertical increases from 40 m close to the ground to 1000 m. The upper boundary is located at 11500 m. A total of $51 \times 51 \times 25$ grid points is used for the simulations. Figure 5 shows the gridded values of the topography in the solution domain. The distribution of the different land uses are given in gridded form in Figure 6. For easier discrimination all classes are grouped into 5 types (see legend of Figure 6 for details). One easily

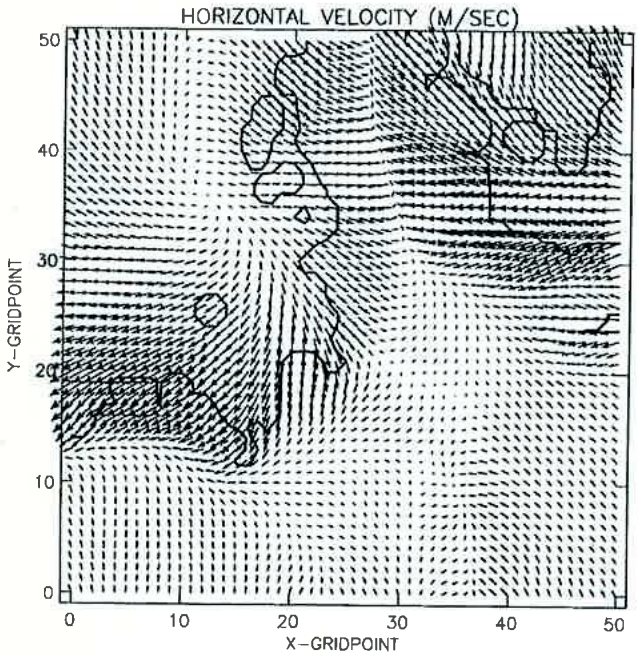

Figure 7 Horizontal wind field 20 m above ground at 18.00 local time for a southerly geostrophic wind of 2 m/s. Arrow length of one grid box length corresponds to a speed of 2 m/s. Maximum wind speed is 5.0 m/s. Coast line is contoured for orientation.

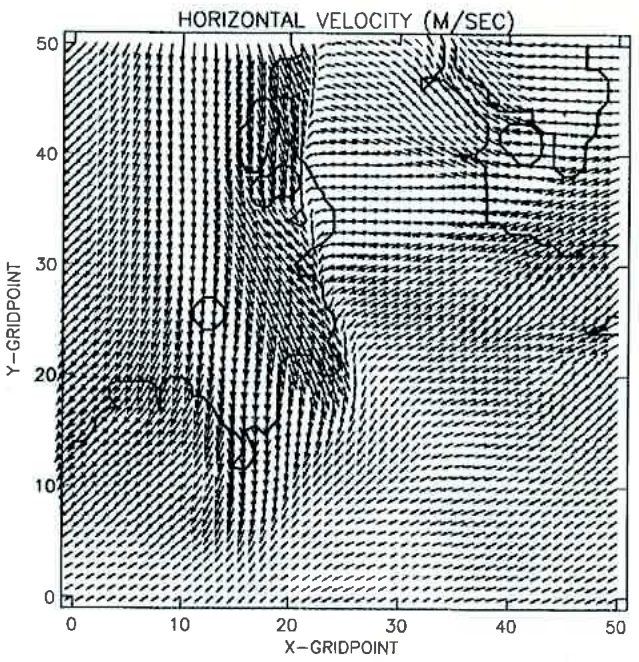

Figure 8 Same as Figure 7, except for easterly geostrophic wind. Maximum wind speed is 5.2 m/s.

recognizes the dry soils (class 16) located along the centerline of Schleswig-Holstein. The south of the solution domain consists mainly of forests (class 6). The influence of the temporal variation of the tide on the sea breeze (see e.g. Kessler et al. (1985) and Schlünzen (1990)) is neglected. The tidal mudflats are either totally covered with water (at high tide) or water free (at low tide). For the application described here only flood conditions are used.

The synoptic situation around the 23rd of June 1981 indicated little synoptic forcing: a stable high pressure zone extended from Finland through Southern Sweden to Central Europe accompanied by a weak synoptic wind from about South-East of less than 2 m/s. There was little change in the synoptic situation for several days. Therefore, the geostrophic wind of 2 m/s prescribed in the model was kept constant throughout the simulations.

The model was initialized for midnight according to the procedure described in Section 3.1. As the external forcing was weak and not well determined two simulations were performed. One case with a southerly geostrophic wind of 2 m/s, the other case with an easterly geostrophic wind of the same magnitude. Due to the initialization procedure and due to the start time at midnight the model did not need a long adaption phase to reach a balanced state between local and external forcing.

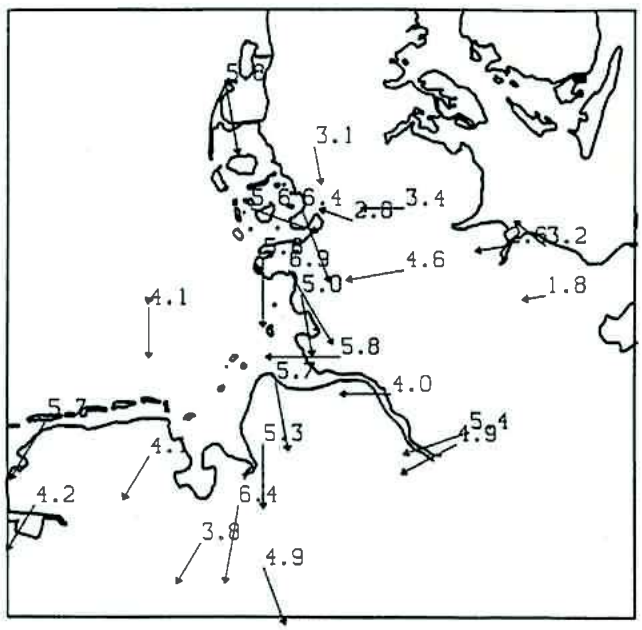

Figure 9 Hourly wind measurements in m/s of the German Weather Service at 18.00 on June 23rd, 1981 (from the KFKI-project "Seegang und, Bemessung auf Seegang im Küstenvorfeld der Deutschen Bucht und in den Ästuaren").

In Figures 7 and 8 the wind fields for the two cases are shown at 20 m above ground and 18 hours after the start of the model. In the case with southerly geostrophic wind (Figure 7) two significant convergence zones developed, one located over central Schleswig-Holstein and the other over the northern

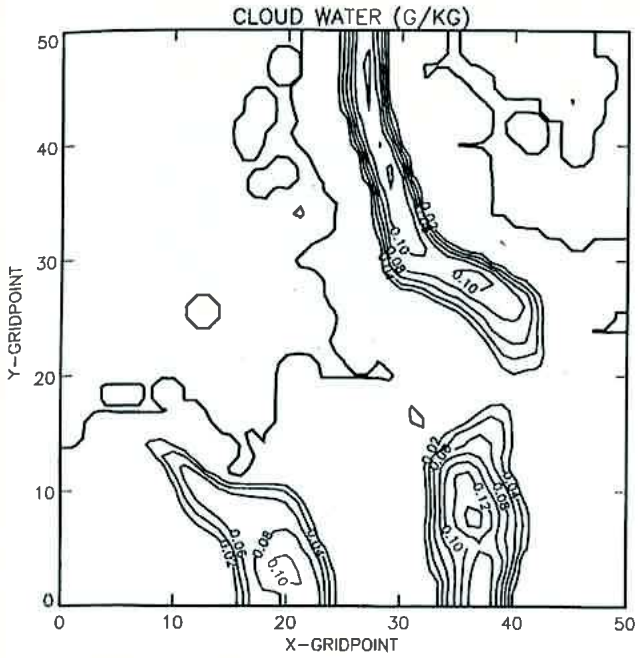

Figure 10 Cloud liquid water content q_l in g/kg at 1300 m above ground for a southerly geostrophic wind of 2 m/s and a local time of 18.00. The coast line is included as a thick contour for orientation.The contour increment is 0.02 g/kg, and the maximum value is 0.145 g/kg.

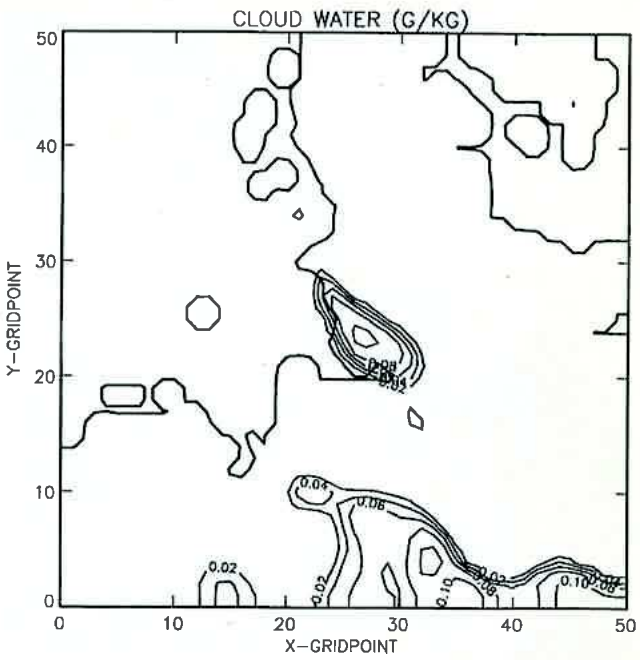

Figure 11 Same as Figure 10, except for easterly geostrophic wind. The maximum value is 0.110 g/kg.

part of Ostfriesland close to the southern coast of the North Sea. This pattern of convergence zones is altered considerably by prescribing an easterly geostrophic wind. The convergence zone over Schleswig-Holstein has now shifted to the North-Sea coast, and in the southern part only some diffuse areas of convergence are visible. Hourly surface winds of the "Deutscher Wetterdienst" (Figure 9) show a similar pattern as our results for easterly flow (Figure 8). The abrupt change of wind direction along the western coast of Schleswig-Holstein (indicative of the convergence zone) is quite obvious. It is also seen from Figure 9 that for the southern coast of the North Sea no such clear front position can be detected. Our results show somewhat higher wind speeds particularly along the coast of the Baltic Sea. The reason for that is not quite clear. It can be a result of different reference heights between our model, which has its lowest level at 20 m for this application, and the measuring sites, which usually use 10 m for wind observations. Furthermore, the measurements are hourly means while our results are means over at most one time step (10 seconds in this case). Also, our assumption of a steady and over the model domain homogeneous synoptic situation might simply be wrong. Nevertheless, the qualitative agreement between model results and measurements is quite good.

The difference of flow pattern between southerly and easterly flow can also be detected by the locations of cloud activity over Schleswig-Holstein. For the southerly flow case a coherent cloud band has formed extending all through Schleswig-Holstein (Figure 10) only interrupted around y-gridpoint 20. Along the southern North Sea coast the updraft is not quite strong enough to start cloud development which can be seen from the vertical velocity distribution (not presented here). For easterly flow (Figure 11) a cloud cluster is found north of the Elbe estuary which is in qualitative agreement with the AVHRR NOAA6 satellite picture shown in Figure 12. Cloud activity was confined to a slab between 1100 m and about 1500 m and no ice formation was detected in the model. These results are in good agreement with the temperature data at cloud top determined from the satellite data. In the southern part of the model domain a large cloud covered area is seen which is not related to any convergence zone (compare Figure 8). This area results from the fact that during daytime the land mass generates a lot of moisture by evaporation from soil and vegetation. This moisture is mixed vertically throughout the boundary layer by subgrid convection. Near the top of the boundary layer located at about 1700 m it is moist and cold enough to start condensation. This process happens

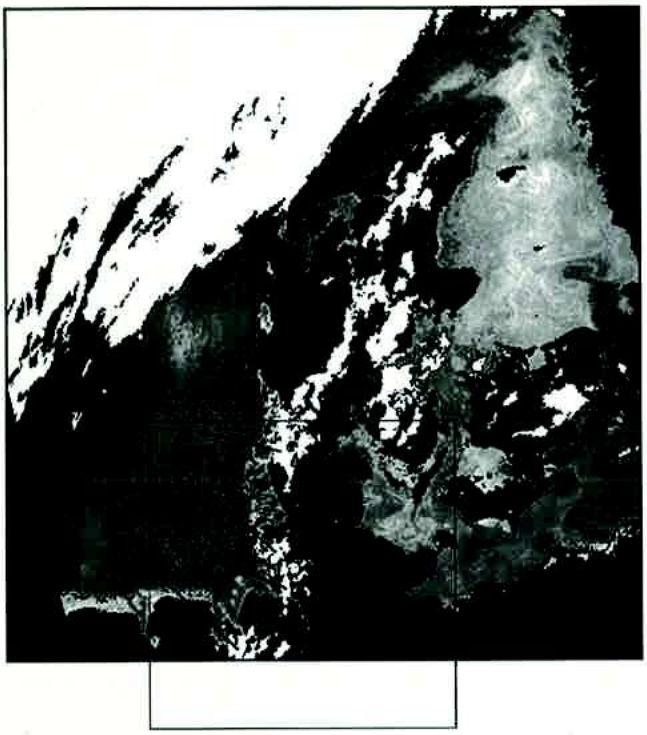

Figure 12 AVHRR NOAA 6 satellite image at 17.34 GMT of June 23rd, 1981. The box indicates the computational domain. The numbers represent cloud top temperatures in °C.

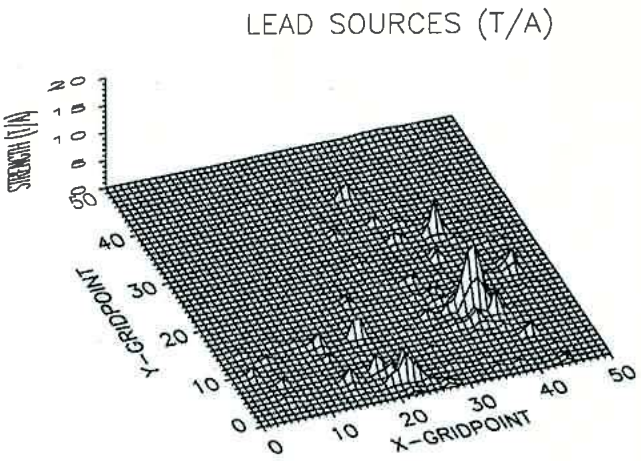

Figure 13 Perspective view of areal lead source distribution in tons/year (t/a). The highest values are for the Hamburg area with a peak of 11 t/a.

only in the south because only there all transported air masses have their origin over land containing similar amounts of moisture. Near the coast maritime air is advected by the sea-breeze which is moist only near the surface because of suppressed vertical mixing due to the stable stratification over the relatively cold water. In those areas clouds are only generated when supported by updrafts due to low-level convergence.

6.4 Pollutant Transport over Northern Germany

For the same solution domain the transport of atmospheric lead resulting mainly from traffic is simulated. The lead particles are assumed to be small enough to float freely in the transporting air mass. Therefore, using an equation in analogy to Eq. (3.3) is justified. Similar to the definition of cloud water droplets the terminal fall velocity of lead particles is neglected. A winter episode (January, 16 to 18, 1987) is chosen which is similar in its synoptic characteristics to the sea-breeze simulation described in Section 6.3. The land areas are snow-covered which strongly affects emissivities, albedo and latent heat fluxes. The sea surface temperatures are kept constant at 0 °C. Due to the extremely cold temperatures (dropping below –20 °C during night time) a very stable stratification develops which restricts the transport of pollutants to the lowest 300 m of the atmosphere. The blocking conditions over several days prevent the development of appreciable daily variations in the meteorological variables. An estimated synoptic wind of 2 m/s from south-east is used as upper boundary condition. Since no clouds were observed during the period considered the cloud module was turned off and the cloud cover parameter N_c (see Chapter 4) was set to zero.

Investigations on transport, transformation and deposition are usually hampered by insufficient knowledge of the sources in- and outside the solution domain. Or, the emission database lacks behind several years. Emission inventories for trace metals have been developed since several years, and among the most reliable is the one for particulate lead. The emission inventory used for this investigation has been prepared by Münch and Axenfeld (1990) for the year 1987. Annually averaged source strengths of lead resulting from industrial production, households, waste disposal and traffic are given for 5×5 km^2 areas. Traffic contributes more than 90 % of the total emission. The emissions are subdivided into particles with diameters of 0–1 μm, 1–10 μm, and > 10 μm, respectively. As the main fraction of lead is concentrated around the 1 μm particles (Graßl et al., 1989) the calculations were performed with an average particle size of 1 μm. In Figure 13 the total area source distribution is depicted. As can be expected the high emissions coincide with the major cities. Emission heights for

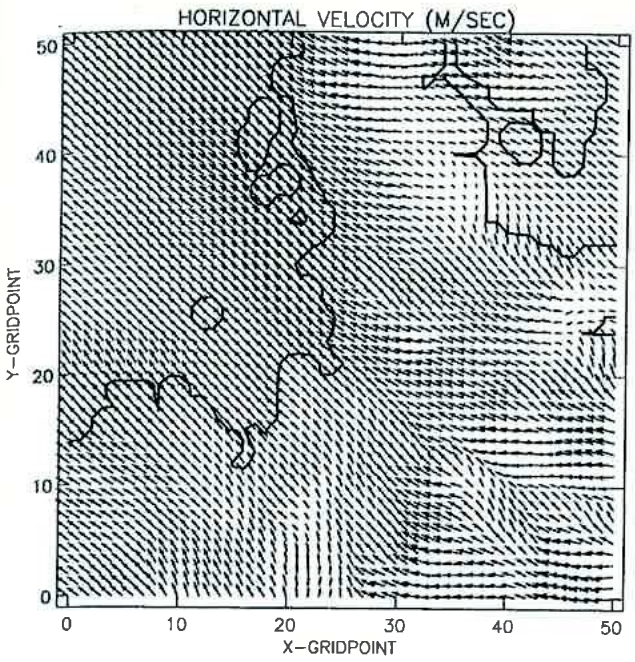

Figure 14 Like Figure 7, at 12.00 of the second day of the winter simulation. Maximum wind speed is 3.8 m/s.

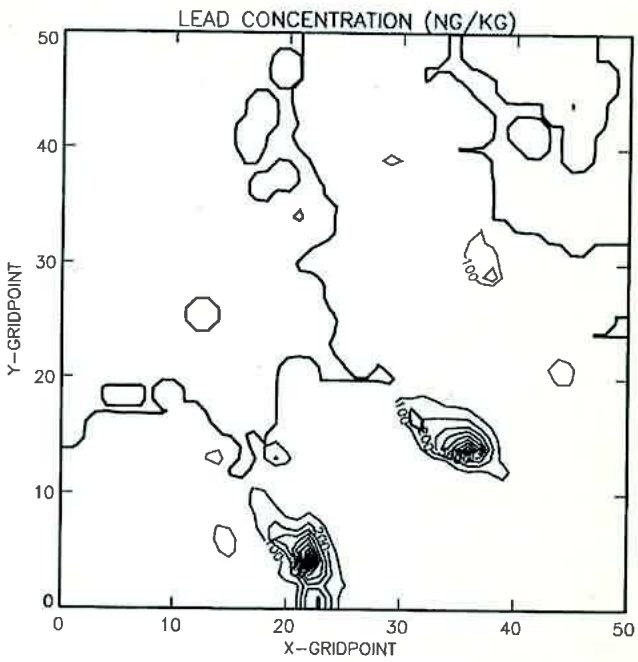

Figure 15 Lead concentration 20 m above ground at 12.00 of the second day. The coast line is shown in thick contours for orientation. The contour increment for lead is 100 ng/kg, the maximum value is 988 ng/kg.

traffic are set to 1 m above ground, for households and industry to 20 m, and for dumping sites to 5 m. There is no diurnal variation in the emissions as the emission inventory represents annually averaged quantities. Possible temporal variations are therefore solely due to changes in the meteorological conditions.

Sources outside the solution domain cannot be neglected. Therefore, a background concentration of 18 ng/kg of atmospheric lead was prescribed. The value was taken from simulation results of the EMEP model (Graßl et al., 1989). In a first simulation with emissions and external forcing turned off a stationary flow field was generated inside the solution domain. The background concentration from EMEP was then inserted and the background deposition distribution was calculated.

The blocking situation together with the strong stratification prevent the development of a diurnal variation of the wind fields worth mentioning. Figure 14 shows the wind field in 20 m above ground 36 hours after model start (noon time). The slight variations in the wind field are caused by orographical variations like the Elbe valley or the hills in the southern part of the solution domain.

With the emissions turned on, a gradual pile-up of concentration and an increase of deposition rates can be seen. After about 20 hours stationary fields of concentration and deposition rates are reached. Figure 15 shows the concentration field in 20 m height above ground 36 hours after model start. As household and small industry emissions are located in this height the concentration field reflects the emission situation. The locations of the densely populated regions reach concentration maxima of almost 1000 ng/kg in the Hamburg area.

The main contributor to the load is traffic as can be expected from the emission inventory. Figure 16 shows the deposition rates due to this inventory 36 hours after model start. It shows local deposition in the vicinity of the emittors with a peak value of approximately 1.5 $\mu g/(m^2 h)$ in the urban area of Hamburg. One interesting feature of Figure 16 is the local deposition maximum of 0.3 $\mu g/(m^2 h)$ over the North Sea. Figure 17 shows the lead concentration at 36 hours for an elevation of 70 m above ground (note the changed scale when comparing with Figure 15). From Figure 17 it is obvious that the local deposition maximum over the North Sea is related to the transport of lead from the Hamburg area. Over the warm water the atmosphere is less stable than over the cold land, which enhances the mixing and results in higher deposition rates.

Figure 18 shows the deposition rates resulting from the "unleaded fuel" scenario. When comparing with Figure 16 (note the changed scale) an overall

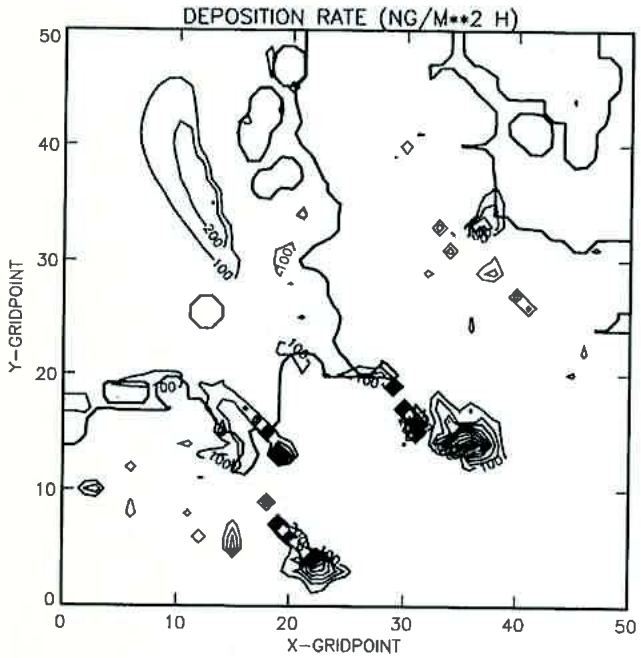

Figure 16 Lead deposition rates at 12.00 of the second day for the "complete inventory" scenario. The coast line is shown in thick contours for orientation. The contour increment for deposition rate is 100 ng/(m^{2}h), the maximum value is 1525 ng/(m^{2}h).

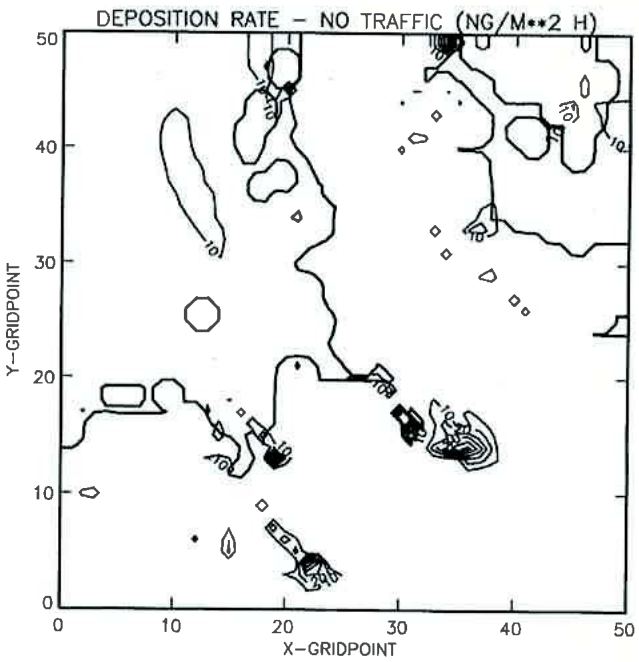

Figure 18 Same as Figure 16, except for "unleaded fuel" scenario. The contour increment is 10 ng/(m^{2}h), and the maximum value is 92 ng/(m^{2}h).

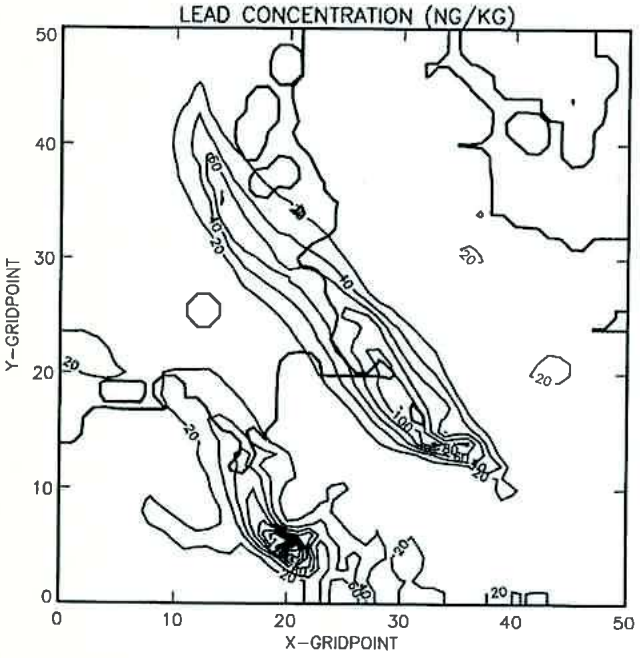

Figure 17 Same as Figure 15, except for 70 m above ground. The contour increment is 20 ng/kg, and the maximum value is 205 ng/kg.

reduction by a factor of approximately 16 is found. There is also a local maximum over the North Sea for the same reason as discussed above.

Comparative studies of lead transport during summer time show (not presented here) that over land the deposition rates in winter and summer are in the same range. The reason for this behaviour might be found in the fact that in summer the concentration is distributed over a thicker mixed layer which reduces the concentration. The deposition velocity is increased due to turbulent mixing. In winter time, the pollutant accumulates in the lower layers of the atmosphere. However, due to both the strong surface inversion and the smooth snow covered surface, comparatively little pollutant is deposited. Over water, deposition is increased in winter time due to the process explained above.

7 Conclusion

The parameterizations used in GESIMA have been discussed and some applications have shown that the model system is able to generate physically reasonable results. Comparisons with measurements (where available) are very promising. Though versions of GESIMA with more advanced parameterizations exist, the reference model needs to be improved in the future. The main shortcomings can be summarized as follows:

- The model is driven with a pre-specified geostrophic wind both constant in space and time. This restricts the application to synoptic situations with little variation, e.g. blocking high pressure systems. One of the next improvements of the model must be the ability to be driven with external boundary values supplied by large-scale models (nesting).
- The cloud module definitely needs some improvement. For example, the ventilation coefficients used for the processes of rain evaporation and snow melting are different since they come from different parameterizations. This should be made consistent in the future. Furthermore, only one ice species is considered in the cloud physics module. This has not been any problem in the application with clouds presented here since in that case only very shallow clouds without ice phase are observed. An extended cloud module has been published by Levkov et al. (1992) applying the model to situations with cirrus and stratus clouds. Further improvements should also make a realistic simulation of the hail generation process in cumulus clouds possible. Relaxation of the assumption of constant droplet distribution parameter ν is highly desirable.
- The shortwave radiative transfer is modelled only for the scattering process. In particular, no heating/cooling rates at cloud top level are possible yet since shortwave absorption is neglected. It seems worthwhile to have the shortwave spectral range treated with similar complexity as the infrared region, i.e. with a two-stream approximation. It might be even necessary for applications with complicated cloud configurations to treat the radiation interaction with a six-stream method, i.e. relaxing the horizontal homogeneity assumption used for deriving the two-stream method. However, this is computationally very expensive.
- The initialization method discussed in this paper needs improvement for applications with steep topography and/or with real-world non-homogeneous initial fields. The ultimate goal is to have a procedure which initializes the model variables based on the adjoint method (Kapitza, 1991), which at the same time allows to derive model sensitivities with respect to specified parameters. This method adopts a phase-space view where the momentary state of the model is a point in phase-space and where the temporal evolution of the model defines a trajectory. The aim of the initialization is to find the starting point of the optimal trajectory defined by minimizing a distance functional J to data. The data themselves are points with a time label in phase-space. The minimization strategy rests on the availability of the gradient of the distance J with respect to the unknown initial state. Once the gradient is known, which is obtained by solving the adjoint model, a better guess to the initial state can be found. Since the adjoint of a model is of similar complexity as the original model, the total cost of finding the gradient is one forward run with the original model and one backward run with the adjoint. The technique just described has been implemented for the dry adiabatic version of GESIMA and has shown promising results as documented in Kapitza (1991).
- The equation for turbulent kinetic energy needs additional terms when the model is going to be applied to cases with very steep and mesoscale-γ topography or for large eddy simulations. In those cases the small aspect ratio argument does not hold anymore and the formulation of the turbulent fluxes needs to be worked over.
- The inconsistency of not using the integrated Businger functions for calculating the turbulent surface fluxes should be resolved in future versions of the model although the effect is believed to be small as discussed in Section 5.
- The surface module needs some refinement. So far, only one surface characteristic is allowed per grid cell. In the future, a distribution of different characteristics within one cell should be allowed resulting in more realistic behaviour of the surface variables in cases of fairly large horizontal grid sizes.
- Furthermore, only dry deposition is simulated for passive constituents. For the cases considered here this approach is sufficient since no clouds were observed during the relevant periods. For more realistic pollutant simulations under wet conditions it is necessary to extend the deposition mechanism with cloud scavenging.

Acknowledgement

This work was partially funded by Federal Environmental Agency (Umweltbundesamt) as R & D project 104 02 583 within the framework of the Environmental Research Plan of the German Federal "Ministry of the Environment, Nature Protection and Nuclear Safety". The long-wave radiation code was kindly provided by Dr. S. Bakan from the

Max-Planck-Institute for Meteorology in Hamburg. The satellite image was prepared by C. Brockmann. We also thank the German Weather Service for providing the hourly surface wind data. Numerous discussions with Prof. H. Graßl are gratefully acknowledged. Last but not least we want to thank two anonymous reviewers for their valuable comments helping to improve this paper.

List of Symbols

Symbol	Description	Value	Unit
a_h	Constant for bluff roughness elements (heat)	39.53	–
a_k	Weight of spectral interval k	–	–
a_q	Constant for bluff roughness elements (moisture)	36.34	–
A'	Empirical constant for rain water freezing	0.66	K^{-1}
b_k	Mass absorption coefficient of spectral interval k	–	$m^2 kg^{-1}$
B	Half space integrated Planck source term	–	$W m^{-2}$
B_W	Planck source term in the window region	–	$W m^{-2}$
B_z	Vertical gradient of B	–	$W m^{-3}$
B^+	B at upper boundary of layer with thickness Δz	–	$W m^{-2}$
B^-	B at lower boundary of layer with thickness Δz	–	$W m^{-2}$
B'	Empirical constant for rain water freezing	100	$m^{-3} s^{-1}$
C_d	Transfer coefficient for momentum	–	–
C_h	Transfer coefficient for heat	–	–
C_q	Transfer coefficient for moisture	–	–
C_s	Transfer coefficient for passive constituents	–	–
c	Empirical coefficient for ice crystal fall speed	4.836	$m^{1-d} s^{-1}$
c_0	Coefficient for $l\sqrt{e}$ parameterization	0.4	–
c_{0h}	Constant for c_h	5.3	–
c_{0m}	Constant for c_m	7.4	–
c_{0q}	Constant for c_q	5.3	–
c_1	Constant for z/L-calculation in unstable domain	0.0284	–
c_2	Parameter for z/L-calculation in unstable domain	–	–
c_3	Parameter for z/L-calculation in unstable domain	–	–
c_h	Coefficient for F_h	–	–
c_m	Coefficient for F_m	–	–
c_p	Specific heat of dry air at constant pressure	1003	$J kg^{-1} K^{-1}$
c_q	Coefficient for F_q	–	–
c_ε	Constant for dissipation term in turbulent energy equation	0.064	–
d	Empirical exponent for ice crystal fall speed	0.25	–
D	Rain drop or ice crystal diameter	–	m
d_1	Parameter for z/L-calculation in stable domain	–	–
d_2	Parameter for z/L-calculation in stable domain	–	–
d_3	Parameter for z/L-calculation in stable domain	–	–
e	Turbulent kinetic energy	–	$m^2 s^{-2}$
e_i	Saturation water vapor pressure over ice	–	Pa
e_l	Saturation water vapor pressure over water	–	Pa
E_c	Collection efficiency of rain for cloud water	1	–
E_S	Collection efficiency of snow for cloud water	1	–
f_v	Ventilation factor for rain drop evaporation	–	–
f_0	Relative terminal velocity reduction of ice particles	–	–
$F\uparrow$	Upward long-wave radiation flux	–	$W m^{-2}$
$F^+_\uparrow$	$F\uparrow$ at upper boundary of layer with thickness Δz	–	$W m^{-2}$
$F^-_\uparrow$	$F\uparrow$ at lower boundary of layer with thickness Δz	–	$W m^{-2}$
$F\downarrow$	Downward longwave radiation flux	–	$W m^{-2}$
$F^+_\downarrow$	$F\downarrow$ at upper boundary of layer with thickness Δz	–	$W m^{-2}$

Symbol	Description	Value	Unit
$F_{\downarrow}$	$F_{\downarrow}$ at lower boundary of layer with thickness Δz	–	$W\,m^{-2}$
$F_{\downarrow,G}$	Long wave counter radiation flux at the surface	–	$W\,m^{-2}$
F_N	Net long-wave radiation flux	–	$W\,m^{-2}$
F_h	Stability function for heat	–	–
F_m	Stability function for momentum	–	–
F_q	Stability function for moisture	–	–
F_s	Turbulent flux of passive constituent	–	$kg\,m^{-2}s^{-1}$
$\mathbf{F}$	Contravariant mass flux	–	$kg\,s^{-1}$
$\mathbf{F}_{s,j}$	Contravariant mass flux of q_j due to fallout	–	$kg\,s^{-1}$
g	Gravity acceleration	9.81	$m\,s^{-2}$
$g\,(\ldots)$	Stomata reaction function	–	-
g_s	Canopy conductance	–	$m\,s^{-1}$
g_1	Maximum surface evaporation conductivity	–	$m\,s^{-1}$
J	Determinant of Jacobian of coordinate transformation	–	m^3
k	Temperature diffusivity of soil	–	m^2s^{-1}
K_a	Thermal conductivity of air	0.0243	$J\,m^{-1}s^{-1}K^{-1}$
K_{ij}	Turbulent momentum exchange coefficient tensor	–	m^2s^{-1}
K_{H1}	Horizontal turbulent exchange coefficient for heat	–	m^2s^{-1}
K_{H3}	Vertical turbulent exchange coefficient for heat	–	m^2s^{-1}
K_{M1}	Horizontal turbulent exchange coefficient for momentum	–	m^2s^{-1}
K_{M3}	Vertical turbulent exchange coefficient for momentum	–	m^2s^{-1}
l_m	Mixing length	–	m
L	Monin-Obukhov length scale	–	m
L_C	Latent heat of condensation	$2.5 \cdot 10^6$	$J\,kg^{-1}$
L_F	Latent heat of fusion	$3.11 \cdot 10^5$	$J\,kg^{-1}$
L_S	Latent heat of sublimation	$2.83 \cdot 10^6$	$J\,kg^{-1}$
L_w	Liquid water path	–	$kg\,m^{-2}$
L_λ	Spectral infrared radiation density	–	$W\,m^{-2}$
$L_{\lambda,B}$	Source term in radiative transfer equation	–	$W\,m^{-2}$
m	Absorber mass	–	$kg\,m^{-2}$
m_w	Soil moisture availability	–	–
n_i	Marshall-Palmer distribution function for ice crystals	–	m^{-4}
n_r	Marshall-Palmer distribution function for rain drops	–	m^{-4}
n_{0i}	Intercept parameter of n_i	$3 \cdot 10^6$	m^{-4}
n_{0r}	Intercept parameter of n_r	$8 \cdot 10^6$	m^{-4}
N	Number concentration of cloud droplets	–	m^{-3}
N_a	Number of long-wave spectral intervals	–	–
N_c	Fractional cloud cover	–	–
N_d	Number of the day in the year	–	–
p	Pressure	–	Pa
p_{00}	Reference pressure	10^5	Pa
P	Precipitation mass flux	–	$kg\,m^{-2}s^{-1}$
Pr	Prandtl number	–	–
q_i	Cloud ice mixing ratio	–	$kg\,kg^{-1}$
q_i^*	Saturation water vapor mixing ratio over ice	–	$kg\,kg^{-1}$
q_l	Cloud liquid water mixing ratio	–	$kg\,kg^{-1}$
q_l^*	Saturation water vapor mixing ratio over water	–	$kg\,kg^{-1}$
q_r	Rain water mixing ratio	–	$kg\,kg^{-1}$
q_v	Water vapor mixing ratio	–	$kg\,kg^{-1}$
$q_{v,G}$	Surface water vapor mixing ratio	–	$kg\,kg^{-1}$
$q_{vs,G}$	Saturation surface water vapor mixing ratio	–	$kg\,kg^{-1}$
q_v^*	Saturation water vapor mixing ratio in mixed phase range	–	$kg\,kg^{-1}$

Symbol	Description	Value	Unit
Q_{ground}	Sensible ground heat flux	–	$W\,m^{-2}$
Q_{lat}	Latent heat flux	–	$W\,m^{-2}$
Q_{rad}	Radiation heat flux	–	$W\,m^{-2}$
Q_{sens}	Sensible heat flux	–	$W\,m^{-2}$
Q_{AU}	Autoconversion of cloud water to rain drops	–	$kg\,kg^{-1}\,s^{-1}$
Q_{CN}	Condensation/Evaporation of cloud water	–	$kg\,kg^{-1}\,s^{-1}$
Q_{DE}	Deposition/Sublimation of ice	–	$kg\,kg^{-1}\,s^{-1}$
Q_{EV}	Evaporation of rain water	–	$kg\,kg^{-1}\,s^{-1}$
Q_{FR}	Freezing of cloud water	–	$kg\,kg^{-1}\,s^{-1}$
Q_{FW}	Freezing of cloud water	–	$kg\,kg^{-1}\,s^{-1}$
Q_{MS}	Melting of snow	–	$kg\,kg^{-1}\,s^{-1}$
Q_{RAC}	Accretion of rain water with cloud droplets	–	$kg\,kg^{-1}\,s^{-1}$
Q_{SAC}	Accretion of snow with cloud droplets	–	$kg\,kg^{-1}\,s^{-1}$
Q_{q_j}	Source term of q_j-equation (j = i, l, r, v)	–	$kg\,kg^{-1}\,s^{-1}$
Q_θ	Source term of θ-equation	–	$K\,s^{-1}$
r_b	Surface resistance for lead particles	–	$s\,m^{-1}$
R	Gas constant for dry air	287	$J\,kg^{-1}\,K^{-1}$
Ri	Richardson number	–	–
R_i	Snow fall rate	–	$mm\,h^{-1}$
R_r	Rain fall rate	–	$mm\,h^{-1}$
s	Passive constituent mixing ratio	–	$kg\,kg^{-1}$
S_c	Schmidt number (ν_k/Ψ)	0.64	–
S_0	Solar radiation flux at the earth's surface	–	$W\,m^{-2}$
$\overline{S}_0$	Constant in Kasten and Czeplak parameterization	950	$W\,m^{-2}$
$\overline{S}_1$	Constant in Kasten and Czeplak parameterization	30	$W\,m^{-2}$
t	Time	–	s
t_H	Local hour angle	–	deg
t_L	Local time	–	hours
T	Absolute temperature	–	K
T_G	Absolute surface temperature	–	K
T_r	Shortwave transmission function	–	–
T_s	Absolute water surface temperature	–	K
T_0	Upper boundary of mixed phase temperature range	273.16	K
T_{00}	Lower boundary of mixed phase temperature range	238.16	K
$\widetilde{T}$	Longwave transmission function	–	–
u	Horizontal velocity component in x-direction	–	$m\,s^{-1}$
u_i	i-th velocity component	–	$m\,s^{-1}$
u_i'	Fluctuation of i-th velocity component	–	$m\,s^{-1}$
u_*	Friction velocity	–	$m\,s^{-1}$
v	Horizontal velocity component in y-direction	–	$m\,s^{-1}$
V_i	Mean terminal fall speed of snow	–	$m\,s^{-1}$
V_r	Mean terminal fall speed of rain	–	$m\,s^{-1}$
w	Vertical velocity component	–	$m\,s^{-1}$
w_e	Wetness factor	–	–
w_k	Field capacity	–	m
x_i	i-th cartesian coordinate direction	–	m
x	Cartesian coordinate (x_1)	–	m
y	Cartesian coordinate (x_2)	–	m
z	Cartesian height above ground (x_3)	–	m
z_p	Reference height for transfer coefficients	–	m
z_0	Roughness length for momentum	–	m
z_{0h}	Roughness length for heat	–	m

Symbol	Description	Value	Unit
z_{0q}	Roughness length for moisture	–	m
z_{0s}	Roughness length for passive constituent	–	m
z^-	Lower value of z for a layer of thickness Δz	–	m
z^+_{max}	Upper value of z for the highest level	–	m
α	Albedo	–	–
α_c	Capillarity factor	–	$kg\,m^{-3}s^{-1}$
α_e	Coefficient in turbulent energy equation	1.0	–
α_{sea}	Albedo for water	–	–
β	Path elongation factor	1.66	–
β_1	Effective backscatter coefficient	–	–
δ	Declination of the sun	–	deg
δq_v	Water vapor deficit	–	$kg\,kg^{-1}$
Δq_i	Change of q_i by deposition adjustment term	–	$kg\,kg^{-1}$
Δq_l	Change of q_l by condensation adjustment term	–	$kg\,kg^{-1}$
Δq_v	Change of q_v by condensation/deposition adjustment term	–	$kg\,kg^{-1}$
Δt	Model time step	–	s
Δz	Model layer thickness	–	m
ε	Angle of the earth's ecliptic	23.45	deg
ε_e	Emissivity of a surface	–	–
Γ	Gamma-function	–	–
κ	Von Karman's constant	0.35	–
λ	Asymptotic maximum mixing length	–	m
λ_h	Heat conductivity of soil	–	$J\,K^{-1}m^{-1}s^{-1}$
λ_i	Distribution parameter of n_i	–	m^{-1}
λ_r	Distribution parameter of n_r	–	m^{-1}
μ	$\cos(\zeta_{zen})$	–	–
∇_ξ	Operator $\left(\frac{\partial}{\partial\xi}, \frac{\partial}{\partial\eta}, \frac{\partial}{\partial\zeta}\right)$	–	–
ν	Relative dispersion coefficient of cloud droplet distribution	0.28	–
ν_k	Kinematic viscosity of air	$0.1346 \cdot 10^{-4}$	m^2s^{-1}
Φ	Geographical latitude	–	deg
Φ_M	Businger's stability function	–	–
Ψ	Water vapor diffusivity in air	$0.211 \cdot 10^{-4}$	m^2s^{-1}
$\underline{\rho}$	Density of air	–	$kg\,m^{-3}$
$\bar{\rho}$	Density of dry reference atmosphere air	–	$kg\,m^{-3}$
ρ_0	Sea level reference density	–	$kg\,m^{-3}$
ρ_i	Density of ice	100	$kg\,m^{-3}$
ρ_w	Density of water	1000	$kg\,m^{-3}$
σ	Spectral extinction coefficient	–	m^{-1}
σ_{cont}	Continuum mass absorption coefficient	–	m^2kg^{-1}
σ_d	Liquid water extinction coefficient	50	m^2kg^{-1}
σ_s	Stefan-Boltzmann constant	$5.6693 \cdot 10^{-8}$	$W\,m^{-2}K^{-4}$
Σ_{q_j}	Part of turbulent flux vector of q_j	–	m^3s^{-1}
τ	Turbulent momentum flux	–	$kg\,m^{-1}s^{-2}$
τ_{ij}	Mean correlation of u_i' and u_j'	–	m^2s^{-2}
τ_1	Cloud optical thickness	–	–
Θ	Potential temperature	–	K
ξ	1st coordinate in computational domain (= ξ_1)	–	–
ξ_i	i-th coordinate in computational domain	–	–
ξ_x	$\partial\xi/\partial x$	–	m^{-1}
ξ_y	$\partial\xi/\partial y$	–	m^{-1}
ξ_z	$\partial\xi/\partial z$	–	m^{-1}

Symbol	Description	Value	Unit
η	2nd coordinate in computational domain (= ξ_2)	–	–
η_x	$\partial\eta/\partial x$	–	m^{-1}
η_y	$\partial\eta/\partial y$	–	m^{-1}
η_z	$\partial\eta/\partial z$	–	m^{-1}
ζ	3rd coordinate in computational domain (= ξ_3)	–	–
ζ_x	$\partial\zeta/\partial x$	–	m^{-1}
ζ_y	$\partial\zeta/\partial y$	–	m^{-1}
ζ_z	$\partial\zeta/\partial z$	–	m^{-1}
ζ_{zen}	Zenith angle of the sun position	–	deg
$\langle . \rangle$	Ensemble mean (Reynolds averaging)	–	–

References

Atkinson, B. W., 1981: Meso-scale Atmospheric Circulation. Academic Press, New York.

Bakan, S., 1994: A simple radiation parameterization for use in mesoscale models. MPI-Report (in press).

Berry, E. X., 1967: Cloud droplet growth by collection. J. Atmos. Sci. **97,** 688–701.

Berry, E. X., 1968: Modification of the Warm Rain Process. Proc. First Nat. Conf. Weather Modification, April 28–May 1, Albany, New York, AMS, Boston, Mass. 81–88.

Bigg, E. K., 1953: The supercooling of water. Proc. Phys. Soc. London **B66,** 688–694.

Blackadar, A. K., 1962: The vertical distribution of wind and turbulent exchange in a neutral atmosphere. J. Geophys. Res. **67,** 3095–3102.

Blanc, T. V., 1982: Profile-bulk formulas for calculating flux and stability in the marine atmospheric surface layer and a survey of field experiments. Naval Research Laboratory, NRL Report 8647, Washington, D.C., 17 p.

Bougeault, P. and *P. Lacarrere,* 1989: Parameterization of orography-induced turbulence in a mesobeta scale model. Monthly Wea. Rev. **117,** 1870–1888.

Brutsaert, W., 1979: Heat and mass transfer to and from surfaces with dense vegetation or similar permeable roughness. Boundary-Layer Meterology **16,** 365–388.

Businger, J. A., J. C. Wyngaard, Y. Izumi and *E. F. Bradley,* 1971: Flux-profile relationships in the atmospheric surface layer. J. Atmosph. Sci. **28,** 181–189.

Buykov, M. V. and *V. I. Khvorostyanov,* 1977: Formation and Evolution of Radiation Fog and Stratus Clouds in the Atmospheric Boundary Layer. Izv. Atmosph. Oz. Phys. (Engl. Ed.) **13,** 251–260.

Charnock, H., 1955: Wind stress on a water surface. Quart. J. Roy. Meteorol. Soc. **81,** 639–640.

Claussen, M., 1988: On the surface energy budget of coastal zones with tidal flats. Beitr. Phys. Atmosph. **61,** 39–49.

Claussen, M., 1990: Area-averaging of surface fluxes in a neutrally stratified, horizontally inhomogeneous atmospheric boundary layer. Atmosph. Environ. **24A,** 1349–1360.

Cotton, W. R., M. A. Stephens, T. Nehrkorn and *G. J. Tripoli,* 1982: The colorado state university three-dimensional cloud/mesoscale model-1982. Part II: An ice phase parameterization. Atmosph. Res. **16,** 295–320.

Deardorff, J. W., 1978: Efficient prediction of ground surface temperature and moisture with inclusion of a layer of vegetation. J. Geophys. Res. **83,** 1889–1903.

Dolman, A. J., 1987: Predicting evaporation from on Oak forest. Ph. D. thesis, Rijksuniversiteit de Groningen. 91 p.

Elsässer, W. M., 1942: Heat Transfer by Infrared Radiation in the Atmosphere. Harward. Meteorol. Studies No. 6, Harvard University Press, Cambridge, Mass.

Graßl, H., D. Eppel, G. Petersen, B. Schneider, H. Weber, J. Gandraß, K. H. Reinhard, D. Wodarg and *J. Fließ,* 1989: Stoffeintrag in Nord- und Ostsee über die Atmosphäre. GKSS External Report 89/E/8, available from the authors.

Gryning, S. E., 1985: The ØRESUND Experiment – A Nordic Mesoscale Dispersion Experiment over a Land-Water-Land Area. Bull. Am. Met. Soc. **66,** 1403–1407.

Gunn, K. L. S. and *J. S. Marshall,* 1958: The distribution with size of aggregate snowflakes. J. Meteor. **15,** 452–461.

Hicks, B. B., 1985: Application of forest-atmosphere turbulent exchange information. In: B. A. Hutchison and B. B. Hicks (eds.). The Forest-Atmosphere Interaction 631–644.

Hollweg, H. D., 1989: Line-by-Line Model for the Calculation of Infrared Radiation Fluxes and Cooling Rates in Clear Sky Atmospheres. Max-Planck-Institut für Meteorologie, Hamburg, Report No. 36, 46 p.

Jacob, D., 1991: Numerische Simulation der Wolkenbildung in einer Land-Seewind-Zirkulation. GKSS External Report 91/E/40, available from the author.

Kapitza, H., 1991: Numerical Experiments with the Adjoint of a Nonhydrostatic Mesoscale Model. Monthly Wea. Rev. **119,** 2993–3011.

Kapitza, H. and *D. P. Eppel,* 1992: The Non-Hydrostatic Mesoscale Model GESIMA, Part I: Dynamical Equations and Tests. Beitr. Phys. Atmosph. **65,** 129–146.

Kasten, F. and *G. Czeplak,* 1980: Solar and terrestrial radiation dependent on the amount and type of cloud. Solar Energy **24,** 177–189.

Kessler, E., 1969: On the distribution and continuity of water substance in atmospheric circulation. Met. Mon. **32,** American Met. Soc., Boston, Mass.

Kessler, R. C., D. Eppel, R. A. Pielke and *J. M. McQueen,* 1985: A Numerical Study of the Effects of a Large Sandbar upon Sea Breeze Development. Arch. Met. Geoph. Biocl., Ser A **34,** 3–26.

Levkov, L., D. Eppel and *H. Graßl,* 1986: On the simulation of convective structures. External Report GKSS 86/E/35, Geesthacht, Germany.

Levkov, L., D. Jacob, D. Eppel and *H. Graßl,* 1989: Framework of cloud parameterization including ice for 3-D mesoscale models. External Report GKSS 89/E/7, Geesthacht, Germany.

Levkov, L., B. Rockel, H. Kapitza and *E. Raschke,* 1992: 3D Mesoscale Numerical Studies of Cirrus and Stratus Clouds by Their Time and Space Evolution. Beitr. Phys. Atmosph. **65,** 35–58.

Lin, Y. L., R. D. Farley and *H. D. Orville,* 1983: Bulk Parameterization of the Snow Field in a Cloud Model. J. of Climate and Appl. Met. **22,** 1065–1092.

Lord, S. J., H. E. Willoughby and *J. M. Piotrowicz,* 1984: Role of a Parameterized Ice-Phase Microphysics in an Axisymmetric, Nonhydrostatic Tropical Cyclone Model. J. Atmosph. Sci. **41,** 2836–2848.

Louis, J. F., 1979: A parametric model of vertical eddy fluxes in the atmosphere. Boundary-Layer Meteorology **17,** 187–202.

Marshall, J. S. and *W. M. Palmer,* 1948: The distribution of raindrops with size. J. Meteorol. **5,** 165–166.

Mellor, G. L. and *T. Yamada,* 1974: A hierarchy of turbulence closure models for planetary boundary layers. J. Atmosph. Sci. **31,** 1791–1806.

Mengelkamp, H.-T., 1991: Boundary Layer Structure over an Inhomogeneous Surface: Simulation with a Non-Hydrostatic Mesoscale Model. Boundary-Layer Meteorology **57,** 323–341.

Mortensen, N. G. and *S.-E. Gryning,* 1989: The Øresund Experiment – databank report. NORDFORSK – available from Risø National Laboratory.

Moussiopoulos, N., 1987: An Efficient Scheme to Calculate Radiative Transfer in Mesoscale Models. Environmental Software **2,** 172–191.

Münch, J. and *F. Axenfeld,* 1990: Emissionsdatenbasis für die Untersuchung und Bewertung des Pb-Eintrags über die Atmosphäre in Nord- und Ostsee mit Hilfe eines mesoskaligen Ausbreitungsmodells. Report DO LRH-M3/90, available from the authors.

Murray, F. W., 1967: On the computation of saturation vapor pressure. J. Appl. Meteor. **6,** 203–204.

Ogura, Y. and *T. Takahashi,* 1971: Numerical simulation of the cycle of a thunderstorm cell. Monthly Wea. Rev. **99,** 895–911.

Orville, H. D. and *F. J. Kopp,* 1977: Numerical simulation of the history of a hailstorm. J. Atmosph. Sci. **34,** 1596–1618.

Pielke, R. A., 1984: Mesoscale Meteorological Modelling. Academic Press, Orlando, 612 p.

Roberts, R. E., J. E. Selby and *L. M. Biberman,* 1976: Infrared Continuum Absorption by Atmospheric Water Vapor in the 8–12 μm Window. Appl. Opt. **15,** 2085–2090.

Rodgers, C. D. and *C. D. Walshaw,* 1966: The Computation of Infra-red Cooling Rate in Planetary Atmospheres. Quart. J. Roy. Met. Soc. **92,** 67–92.

Schlamp, R. J., H. R. Pruppacher and *A. E. Hamielec,* 1975: A Numerical Investigation of the Efficiency with which Simple Columnar Ice Crystals Collide with Supercooled Water Drops. J. Atmosph. Sci. **32,** 2330–2337.

Schlünzen, K. H., 1990: Numerical Studies on the Inland Penetration of Sea Breeze Fronts at a Coastline with Tidally Flooded Mudflats. Beitr. Phys. Atmosph. **63,** 243–256.

Stephens, G. L., 1978: Radiation Profiles in Extended Water Clouds. II: Parameterization Schemes. J. Atmosph. Sci. **35,** 2123–2132.

Voldner, E. C., L. A. Barrie and *A. Sirois,* 1986: A literature review of dry deposition of oxides of sulphur and nitrogen with emphasis on long-range transport modelling in North America. Atmosph. Environ. **20,** 2101–2123.

Wilson, M. F., A. Henderson-Sellers, R. E. Dickinson and *P. J. Kennedy,* 1987: Sensitivity of the biosphere-atmosphere transfer scheme (BATS) to the inclusion of variable soil characteristics. J. Climate Appl. Meteor. **26,** 341–362.

Wu, J., 1982: Wind stress coefficients over sea surface from breeze to hurrican. J. Geophys. Res. **87,** 9704–9706.